Molecular dynamics simulation (MDS) to study nanoscale machining processes

Accepted copy

Molecular dynamics simulation (MDS) to study nanoscale cutting processes

Saurav Goel[1*], Saeed Zare Chavoshi[2] and Adrian Murphy[1]

[1]School of Mechanical and Aerospace Engineering, Queen's University, Belfast, BT9 5AH, UK

[2]Centre for Precision Manufacturing, Department of Design, Manufacture and Engineering Management, University of Strathclyde, Glasgow, G1 1XJ, UK

*Corresponding author Tel.: +44 28 9097 5625, Email address: s.goel@qub.ac.uk, Fax: +44 028 9097 4148

Abbreviations:

ABOP	Analytical bond order potential
BOP	Bond order potential
CAT	Crystal analysis tool
d	Uncut chip thickness
DXA	Dislocation extraction algorithm
EAM	Embedded-Atom-Method
Fx	Tangential cutting force
Fy	Thrust force
FEA	Finite element analysis
HPC	High performance computing
LLNL	Lawrence Livermore National Laboratory
MDS	Molecular dynamics simulation
NVE	Microcanonical ensemble
PBC	Periodic boundary conditions
SPDT	Single point diamond turning
SDM	Surface defect machining

SiC	Silicon carbide
TB	Tight binding

1. Introduction

Experimental studies aside from being expensive are constrained by the fact that they do not permit direct observation of events occurring at the atomic level, especially at short timescales of a few femtoseconds. For this reason, molecular dynamics simulation (MDS), a versatile numerical analysis tool has evolved as an appropriate bottom-up simulation approach to investigate atomic scale events. The beauty of MDS is that it is informed by quantum properties thereby revealing discrete atomistic mechanics that is otherwise impossible to be investigated using the conventional engineering toolbox, e.g. finite element analysis (FEA).

One of the principal differences between FEA and MDS is that the nodes and the distances between the nodes in MDS are not selected on an arbitrary basis but on the basis of more fundamental units of the material, namely, position of atom as the nodes and inter-atomic distances as the distance between the nodes. Also, the shape and size of the crystal in MDS is dictated by the crystallographic structure of the material and not arbitrarily, such as triangular or rectangular shapes as in FEM. The implementation of MD simulation was first developed through the pioneering work of Alder and Wainwright in the late 1950s [1] in their study of the interactions of hard spheres. Since then, MDS has transcended the field of ultra precision manufacturing, materials science, physics, chemistry, and tribology and has contributed significantly towards improved understanding of our knowledge in the inaccessible atomic scale regime.

Ultra-precision manufacturing has emerged as a powerful tool for manipulating optical, electrical and mechanical properties of components by changing their surface and sub-surface structure at the nanometre length scale [2]. This technique can be utilized to achieve nanometre level tolerances and optical quality finished surfaces, which is required in products used in the defence and security technologies, plastic electronic devices, low cost photovoltaic cells and next generation displays.

Nanoscale machining in this context is an ultra-precision manufacturing method that is used to fabricate components requiring submicron geometry accuracy and atomically smooth surface finish, such as those employed in the optical, semiconductor and opto-electronics industries. As the nanometric machining process involves removing few atomic layers from the surface, it is extremely difficult to observe the machining process and to measure the process parameters directly from the experiments. Thus, investigation of atomistic processes occurring at such small length scales is more amenable to MDS.

MD simulation was adapted to study ultra-precision machining at Lawrence Livermore National Laboratory (LLNL), USA during the late 1980s [3]. Landman *et al.* [4] and Belak, Shimada and Ikawa [5] pioneered the concept of MD in the framework of contact loading studies followed by Voter et al. [6]. Since then, Shimada and Ikawa [7], Rentsch et al. [8] and Komanduri et al. [9] have contributed significantly to this arena and set a sound foundation for the study of nanometric cutting processes using MD simulation.

Currently, significant work is being undertaken in developing unique algorithms for conducting large scale atomic simulations with the integrated usage of "dislocation extraction algorithm" (DXA) and crystal analysis tool (CAT) [10] for automated identification of crystal defects, dislocation lines and their Burgers Vector from the MDS output data. Further research efforts are being directed to study processes such as hard turning [11-13], thermal spray [14], nanoimpact and nanofatigue [15-16], nanoindentation [17-18] and nanometric cutting [19-23]. The majority of these works are reviewed in two comprehensive review articles [24-25]. For the purpose of brevity, this chapter provides the most relevant information for the scientific community interested in adapting MDS as a tool to study nanoscale machining processes. In this chapter, we will present various aspects of MD simulations including virtual/computer experiments, principles of MD simulation, potential-energy functions, boundary conditions, MD simulation procedures, and a number of relevant examples of MDS studies focused on engineering problems.

2. Principle of MD simulation

The essence of the MD simulation method is the numerical solution of Newton's second equation of motion for an ensemble of atoms where the atoms are assumed to follow Newton's second law as follows:

$$a_{ix} = \frac{F_{ix}}{m_i} = \frac{d^2 x_i}{dt^2} \quad , \quad F_{ix} = -\frac{dV}{dx_i} \tag{1}$$

where a_{ix} represents the i^{th} atom's acceleration in the x direction and m_i is the mass of the i^{th} atom. F_{ix} is the interaction force acting on the i^{th} atom by the j^{th} atom in the x direction, x_i is i^{th} atom's x-coordinate and V is the potential energy function. In MDS, these equations are integrated by numerical techniques for extremely short time intervals (1-100 pico-seconds (ps)); and equilibrium statistical averages are computed as temporal averages over the observation time. To render atomistic simulation studies practical, an interatomic potential function is necessary. During MDS, the interatomic bonding forces (both attractive and repulsive) are defined by an appropriate empirical potential-energy function. The MD simulations can be likened to the dynamic response of numerous nonlinear spring-mass (atoms or positive ions) in a system under an applied load, velocity, or displacement conditions. From this point of view, MD simulation is similar to other analysis that engineers routinely undertake, such as the investigation of vibrations of a mechanical system wherein a series of springless-masses and massless-springs are connected and the response of the system is investigated under given external loading conditions.

Figure 1 shows schematically a computer simulation of the deformation of a workpiece being machined with a diamond cutting edge. Every atom shown in figure 1 is in motion and interacts with neighbouring atoms in a manner that can be determined from the interatomic potential energy function.

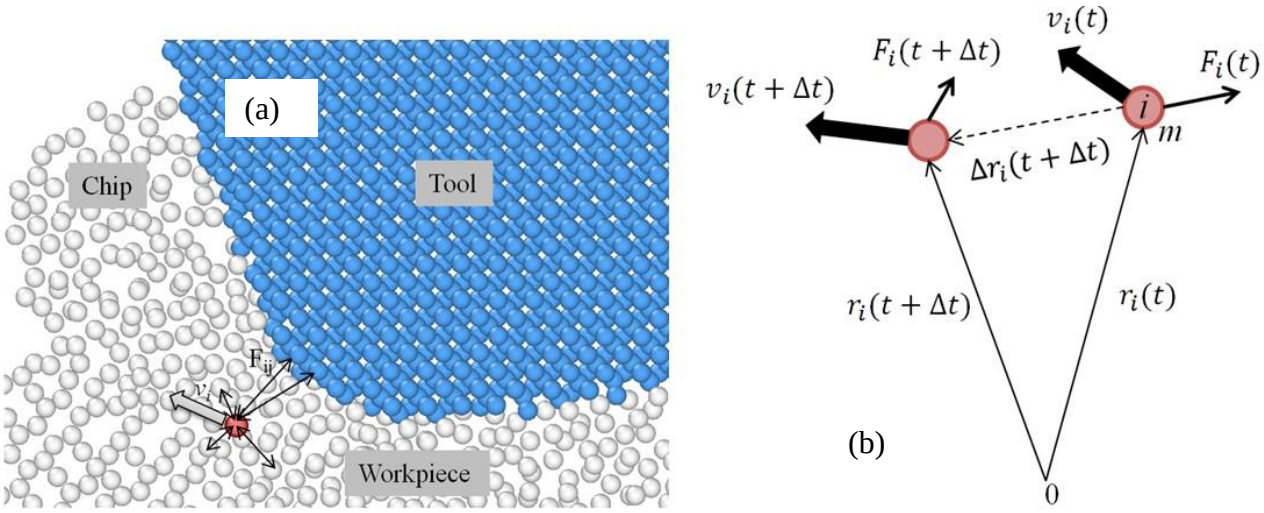

Figure 1: (a) Scheme for performing MD simulation of nanometric cutting (b) an atom 'i' having mass 'm' at a distance of 'r' from the other atom exerts force 'F' on other atom, when given a velocity 'v'

In the simulation, the tool is fed in a stepwise procedure into the workpiece, at time intervals of Δt, that are shorter than the period of lattice vibration. As indicated in Figure 1, the position $r_i(t+\Delta t)$ and velocity $v_i(t+\Delta t)$ of the atom *i* after the tool has been fed in the period of Δt are calculated by employing finite difference method and using Equations (2) and (3). This calculation is then repeated in order to describe the motion of individual atoms. The behaviour of the collection of atoms that comprise the tool/workpiece model can be then analysed through synthesis of the movement of the individual atoms.

$$r_i(t+\Delta t) = r_i(t) + \Delta t v_i(t) + \frac{(\Delta t)^2}{2m} F_i(t) \tag{2}$$

$$v_i(t+\Delta t) = v_i(t) + \frac{\Delta t}{2m}\left[F_i(t+\Delta t) + F_i(t)\right] \tag{3}$$

In general, temperature assessment in an MD simulation is done by averaging the velocity of a group of atoms by using the relationship between kinetic energy and temperature as follows:

$$\frac{1}{2}\sum_i m_i v_i^{\,2} = \frac{3}{2} N k_b T \tag{4}$$

where N is the number of atoms, v_i represents the velocity of i^{th} atom, k_b is the Boltzmann constant (1.3806503×10^{-23} J/K) and T represents the atomistic temperature. The instantaneous fluctuations in

kinetic energy per atom are usually very high so this equation is averaged temporally and/or spatially over a number of time steps and reassigned to each atom at every *N* steps to be converted into equivalent temperature. It may be noted that thermal conduction cannot be analysed correctly in MD simulation, as the normally used potential functions do not take the electron properties into consideration. Since thermal conduction is mainly governed by electron mobility, in practice materials exhibit considerably higher thermal conductivities, and consequently smaller thermal gradients than those estimated by MD simulation based on lattice vibration. Thus, for a more realistic simulation of nanoscale machining, the gradient in thermal field should be scaled, or adjusted, to coincide with that calculated from continuum thermal conduction theory.

2.1. *Potential energy function*

Whenever an atomic scale problem is treated, we require a constitutive description of the atoms. This interaction is governed by a potential energy function that roughly accounts for quantum interactions between electron shells and represents the physical properties of the atoms being simulated, such as its elastic constants and lattice parameters. In general, there are two ways to construct an interatomic potential. The first way is the artistic route of empirical design using chemical and physical insights together with convenient functional forms. The second alternative is the rigorous approach of a bottom-up derivation of the functional forms from a higher level theory, in some cases, tight binding approaches (TB) [26]. Both of these procedures have been applied in the construction of bond order expressions, and both approaches turned out to be largely successful. Potentials used in chemistry are generally called “force fields,” while those used in materials physics are called “analytical potentials.” Most force fields in chemistry are empirical and consist of a summation of forces associated with chemical bonds, bond angles, dihedrals, non-bonding forces associated with van der Waals forces and electrostatic forces.

One of the most successful families of interatomic potentials that have been able to stand the demanding requirement of simultaneous efficiency and reliability is the family of models based on the quantum-mechanical concept of bond order.

Empirical potential-energy functions are classified into two-body potentials, three-body potentials and multi-body potentials, depending on the unit of atoms on which those potentials are based. The potentials which fall into two-body potentials category are Morse, Born-Mayer, Lennard-Jones potentials, etc. The three-body potentials such as Tersoff and analytical bond order potential (ABOP) are devised to represent covalent bonding which has a directional grip and can be used conveniently for material systems involving silicon, germanium, diamond, etc. The multi-body potentials such as Embedded-Atom-Method (EAM) potentials are devised to describe the metallic bonding more accurately than the two-body potentials. AIREBO is another multi-body potential developed to accurately describe hydrocarbons.

In a simple pairwise potential, e.g. Morse or Lennard-Jones potential, only the direct interactions between atoms are considered and summed for a certain sphere with a radius that is usually equal to the spacing between four adjacent atoms. They fully determine the total energy without considering any further cohesive terms that arise from the interaction with atoms far away from the particle considered. The atoms are regarded as mass points which have a central interaction with their nearest neighbours. The interaction of any pair of atoms depends only on their spacing. This implies that such potentials are principally radially symmetric and independent of the angular position of other atoms in the vicinity. The Morse potential function is an example of a pair potential that was frequently used in early research work and is used for simulations even now. It may however be noted that a common limitation of all the pair-potentials is their inability to reproduce the Cauchy pressure, which is a quantity that reflects the nature of the bonding at the atomic level of a material. This was one of the motivations for introducing EAM potential in the year 1984. Unlike Morse potential functions, many of the potentials used in physics, such as those based on bond order formalism, may describe both bond breaking and bond formation (e.g. Tersoff is a three-body potential function, while the AIREBO function is a four-body potential function). Almost all forms of pairwise potentials are empirical due to the approximations necessary to overcome the many-body problem involved in the interaction. The validity of the function, as well as the stability of the

crystal for a given material, are checked for various properties including cohesive energy, the Debye temperature, the lattice constant, the compressibility, and the elastic constants as well as the equation of state. The most widely used bond order potential (BOP) formalism was first proposed by Tersoff [27]. Tersoff based his potential on an idea presented by Abell a few years earlier on BOP, which has environmental dependence and no absolute minimum at the tetrahedral angle. While newly developed formalisms provide greater accuracy, they are sometimes computationally very expensive as shown in table I.

Table I: List of potential functions with respect to the time of introduction

S.No.	Year	Name of the potential function	Materials suited
1	1984	EAM: embedded-atom method [28]	Cu
2	1985	Stillinger-Weber potential [29-30]	Si
3	1987	SPC: simple point charge [31]	H_2O
4	 1988 1988 1989 1990 1994	BOP: bond–order potential • Tersoff-1 variant for silicon [32] • Tersoff-2 for better elastic properties of silicon [27] • Tersoff-3 for Si, C and germanium [33-34] • Tersoff-4 for silicon and carbon [35] • Tersoff-5 for amorphous silicon carbide [36] • Refinements in Tersoff potential function [37-39] • EDIP [40-41]	 Si Si Si, Ge and C Si and C SiC Si and C Si and C
5	1989	MEAM: modified embedded-atom method [42]*	Universal
6	1990	REBO: reactive empirical bond order [43]	Carbon
7	2000	AIREBO: adaptive intermolecular reactive empirical bond order [44] (4 body potential function)	Hydrocarbons and Carbon
8	2001	ReaxFF: reactive force field [45] (Capable of bond breaking and bond-formation during the simulation)	Universal
9	2005	ABOP: analytical bond order potential [46] (3 body potential function)	Si and C
10	2007	COMB: charge optimized many-body [47]	SiO_2, Cu, Ti
11	2008	EIM: Embedded-ion method [48]	Ionic e.g. NaCl
12	2010	GAP: Gaussian approximation potential [49]	Universal
13	1998-2001	Other important potential functions relevant in contact loading problems [50-52]	Si, B and N
14	2013	Screened potential functions [53-54] †	Range of materials

* Latest modifications (2NN MEAM) are available through https://cmse.postech.ac.kr/home_2nnmeam
† Details available from https://github.com/pastewka/atomistica

Tersoff functions gained wide popularity in the 1990s for MD simulations. However, one key drawback of Tersoff (or similar formulations, e.g. Analytical Bond Order Potential (ABOP) [46]) is the way in which the next nearest neighbour atoms are determined, namely *via* a narrow distant-dependent cut-off. In their original incarnation, the artificial abrupt change in energy-distance relation enforces the bond breaking forces to be severely overestimated leading to ductile behaviour in silicon, for example. Consequently, the potential functions proposed by Tersoff and Erhart *et al.* i.e. BOP and ABOP fail to reproduce the density-temperature relation of silicon. This suggests that both BOP and ABOP potential functions are not fully reliable to obtain the phase diagram of silicon. In an attempt to address this problem, a recent effort has been made by decoupling the condition for a nearest-neighbour relationship from the range of the potential [54]. Subsequent refinements have led to a formalism, which is developed by using the screening functions to increase the range of these potentials [53]. By changing the cut-off procedure of all the bond order potential functions, the screening function has been reported to reproduce an improved description of amorphous phases and brittle behaviour of silicon, diamond and silicon carbide. This improvement however has not addressed the problem of obtaining correct melting point of silicon yet and is still a fertile area of research. Overall, Morse potential functions limit the exploration of interaction within atoms of the workpiece and the cutting tool, while Tersoff potential functions have limitations in accurately describing the thermal aspects of silicon which might limit the study of some machining processes related to high temperature applications.

The key message of this section is that a potential energy function is an important consideration for a realistic MD simulation. There are some shortcomings of the currently used potential functions. For example, the ductile-brittle transition during nanometric cutting of silicon and silicon carbide cannot be described well by the Tersoff potential energy function (that has been a heavily used potential function). Similarly, the mechanism of cleavage on certain crystal orientations of brittle materials is yet another aspect that cannot inherently be captured by current potential energy functions [23-24]. Indeed, in absence of crystal orientation information, this was perhaps

misinterpreted as ductile-brittle transition in a previously published study [55]. An important consideration for simulating nanometric cutting of some materials is that the surface bonds or the nascent surface of say, silicon will be reactive and will tend to bond together with the surface of the diamond cutting tool during its approach. In order to avoid such an outcome, it is a good practice to saturate the surface bonds by using hydrogen or any other similar material before the start of the simulation. Finally, MD considers the environment as a vacuum, however the real experimental environment is known to play a key role in influencing the machining outcome and hence a more robust potential function would involve representation of the influence of coolants etc.

2.2.*MD simulation of nanometric cutting*

In what follows, steps involved in an MD simulation are described briefly. Figure 2 provides a general scheme of how an MD simulation of nanometric cutting is performed. This scheme is generic and can well be extended to study other contact loading processes such as nanoindentation, impact loading etc. Also, the description is generalized and may be adapted to any software platform.

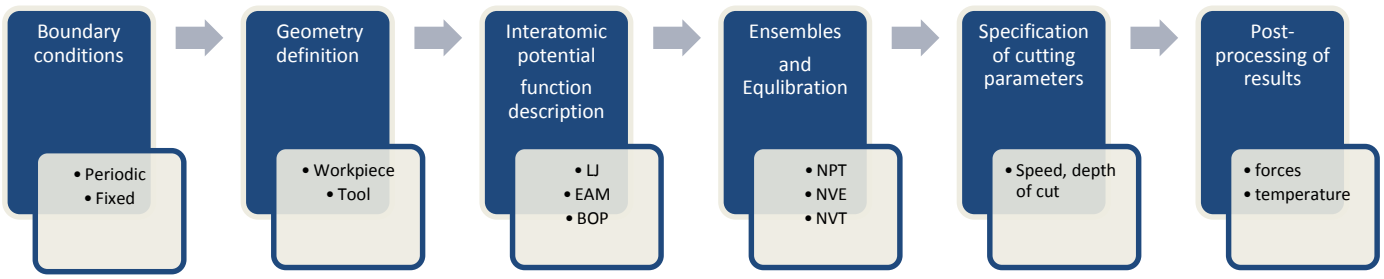

Figure 2: Generic scheme of performing an MD simulation of nanometric cutting

2.2.1. *Boundary conditions and ensemble*

A schematic diagram of the nanometric cutting simulation model is shown in figure 3. In this model, the nano-crystalline workpiece and the cutting tool are modelled as deformable bodies in order to permit tribological interactions between them and to permit the simulation of tool wear. However, if the workpiece is very soft (such as copper and brass), the diamond tool can be modelled as a rigid body since the cutting tool won't wear even after a cutting length of the order of

30 km [56]. The model shown in figure 3 can be seen to have a negative rake angle tool, as this is generally the recommendation for machining of hard and brittle materials.

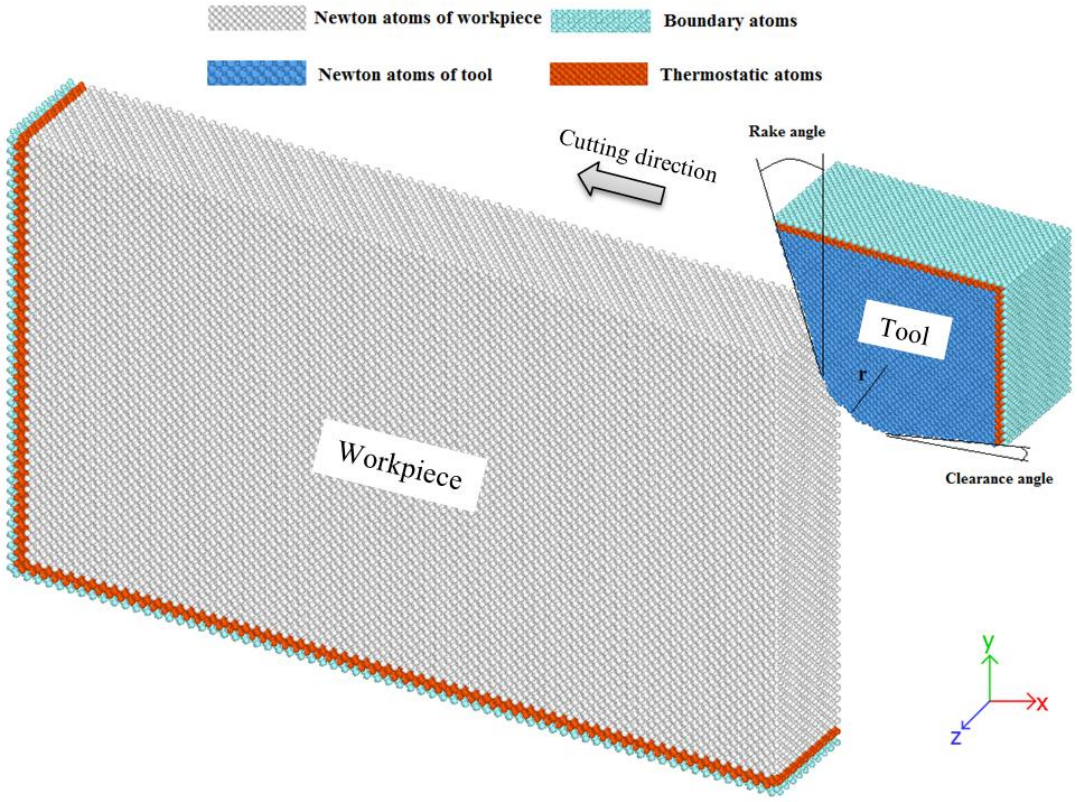

Figure 3: Schematic of MD simulation model

In figure 3, the atoms of the cutting tool and the workpiece are allocated into one of three different zones: Newton atoms, thermostatic atoms and boundary atoms. The boundary atoms are assumed to remain unaffected and fixed in their initial lattice positions during the simulation, serving to reduce the boundary effects and to maintain the symmetry of the lattice. In conventional machining operations, the energy from plastic deformation in the primary shear zone and friction at the tool-chip interface generate heat, which is carried away by chips, lubricant and by conduction into the tool and workpiece. The nanometric cutting model is, however, extremely small and is not capable of dissipating the heat itself. The velocity of the thermostatic atoms is therefore re-scaled to a desired temperature (300K) at each step of the computation to dissipate the artificial heat. It may be noted here that a thermostat layer so close to the cutting zone strongly exaggerates the cooling since it forces that zone to have room temperature. In reality, the thermostat area is at a macroscopic

distance. Such a problem can be handled by either increasing the size of the simulation model both in the X and in the Y direction or by using the multiscale simulation method.

MD simulations are usually implemented considering a system of N particles in a cubic box of length L. Since N is typically in the range of 100 to 10000 (very far from the thermodynamic limits), it is necessary to use periodic boundary conditions (PBC) to avoid surface effects. An important consideration for using PBC is to first determine the equilibration lattice parameter [21]. This could be achieved by averaging the lattice constant from the NPT dynamics ran on a small volume of a material at the desired temperature and pressure for a few femtoseconds. An interesting feature to be noticed here is the adjustment of the lattice constants e.g. nanometric cutting of silicon using a diamond tool involves the use of two different lattice constants i.e. silicon (0.5432 nm) and diamond (0.356 nm). Care must be taken to choose the periodic cell dimensions in such a way that these two lattice constants are in an integer proportion, e.g. $L_z = n_1 \times a_1 = n_2 \times a_2$ where L_z is the box size (in the z direction), n_1 and n_2 are integers and a_1 and a_2 are the two lattice constants. It is generally difficult to find an exact solution to this equation, but for a large enough system, n_1 and n_2 can be approximated reasonably well. Similarly, a change in crystal orientation also requires an adjustment in the dimension of periodic boundary. For example, a workpiece may be positioned on the (111) orientation by specifying the basis vectors in the x direction as (-2 1 1), in the y direction as (1 1 1), and in the z direction as (0 1 -1). An alternative orientation specification could be (-1 1 0), (1 1 1) and (1 1 -2). In both cases, the *z* orientation varies and hence the simulation box size in the z direction should accordingly be adjusted to accommodate the cutting tool and the workpiece. Inappropriately chosen lattice parameters would lead to build-up of excessive stress causing exploding of the atoms before the simulation even begins to run. Once the geometry of a model is ready, the velocities to the atoms can be assigned using the Maxwell-Boltzmann distribution. Followed by an energy minimization, the velocities of all the atoms can be set to a desired temperature. This step is followed by the process of equilibration, wherein, the aim is to achieve a desired temperature until a steady state is achieved. The amount of time required for equilibration

depends on the system being investigated as well as the initial configuration of the system. Newton atoms are then allowed to follow Newtonian dynamics (LAMMPS NVE dynamics), while atoms in an intermediate thin boundary layer were subjected to a thermostat (LAMMPS NVT dynamics) to dissipate the extra heat generated in the finite simulation volume. This consideration of boundary conditions ensures that the process of deformation is not affected by any artificial dynamics.

2.2.2. *Calculation of cutting forces*

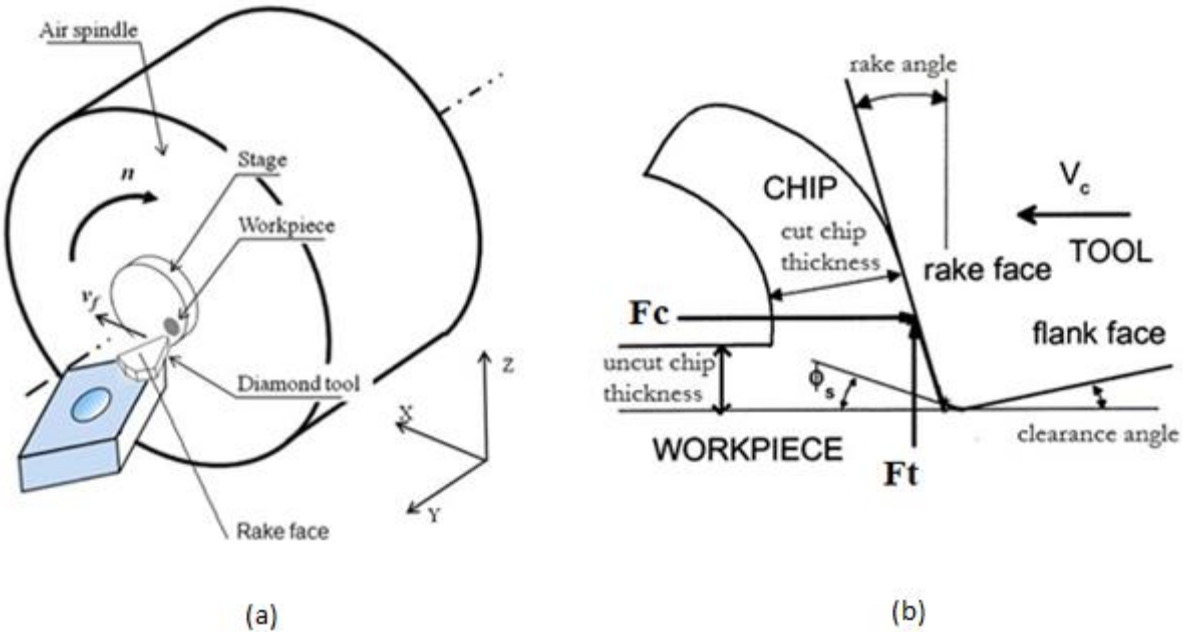

Figure 4: (a) Schematic diagram of chip formation during nanometric cutting [11] and (b) 2D representation of the machining forces acting on the cutting tool

Figure 4 shows schematically the arrangement of nanometric cutting as well as the 2D representation of the two coplanar forces (namely, the tangential cutting force (F_c) and the thrust force (F_t)) acting on a cutting tool fundamentally governing the cutting action of the tool. The third component, F_z acts in the direction orthogonal to the X and Y planes and mainly influences surface error, as it tends to push the tool away from the workpiece. The tangential force causes displacements in the direction of cut chip thickness and its variation therefore relates to chatter. These are the reasons why cutting force measurement is an important indicator of tool wear [57]. From the MD simulation perspective, the calculation of the cutting forces using a diatomic pair potential, such as Morse or Lennard-Jones function is relatively simple because the interaction

energy will include a pair component which is defined as the pairwise energy between all pairs of atoms where one atom in the pair is in the first group (workpiece) and the other is in the second group (cutting tool). These pair interactions can directly be used to compute the cutting forces. For a many-body potential function, such as EAM, Tersoff, ABOP and AIREBO, in addition to the pair-potential, there are other terms that make them computationally expensive. Accounting for these extra terms needs additional computations in addition to those in the pair-wise interactions. Earlier Cai *et al.* [58] have reported that ductile mode cutting is achieved when the thrust force acting on the cutting tool is larger than the cutting force. While this was found to be true in several experimental studies, this is not the case observed during several nanoscale friction based simulation studies where cutting forces are found dominant over thrust forces [59-60]. It is therefore yet another important area for future research.

2.2.3. *Calculation of machining stresses*

The state of stress acting in the machining zone is shown schematically in figure 5 for both 3D and 2D stress systems. One fundamental problem with the computation of atomic stress is that the volume of an atom does not remain fixed during deformation. To mitigate this problem, the best method is to plot the stresses on the fly by considering an elemental atomic volume in the cutting zone. The total stresses acting on that element could be computed and divided by the pre-calculated total volume of that element to obtain the physical stress tensor. Also, the instantaneous values of the stress calculated from the MD simulation should always be time averaged. When a stress tensor from the simulation is available, it can readily be used to obtain the Tresca stress, von Mises stress, Octahedral shear stress and principal stresses.

Overall, MD simulation of nanometric cutting starts with the development of the geometry of the material, and description of the interactions of the atoms with the material using a suitable potential energy function. This is followed by equilibration of the model and simulation in an appropriate ensemble. After the simulation is over, atomic trajectories can be used for post processing of the results (with or without time averaging depending on the quantity).

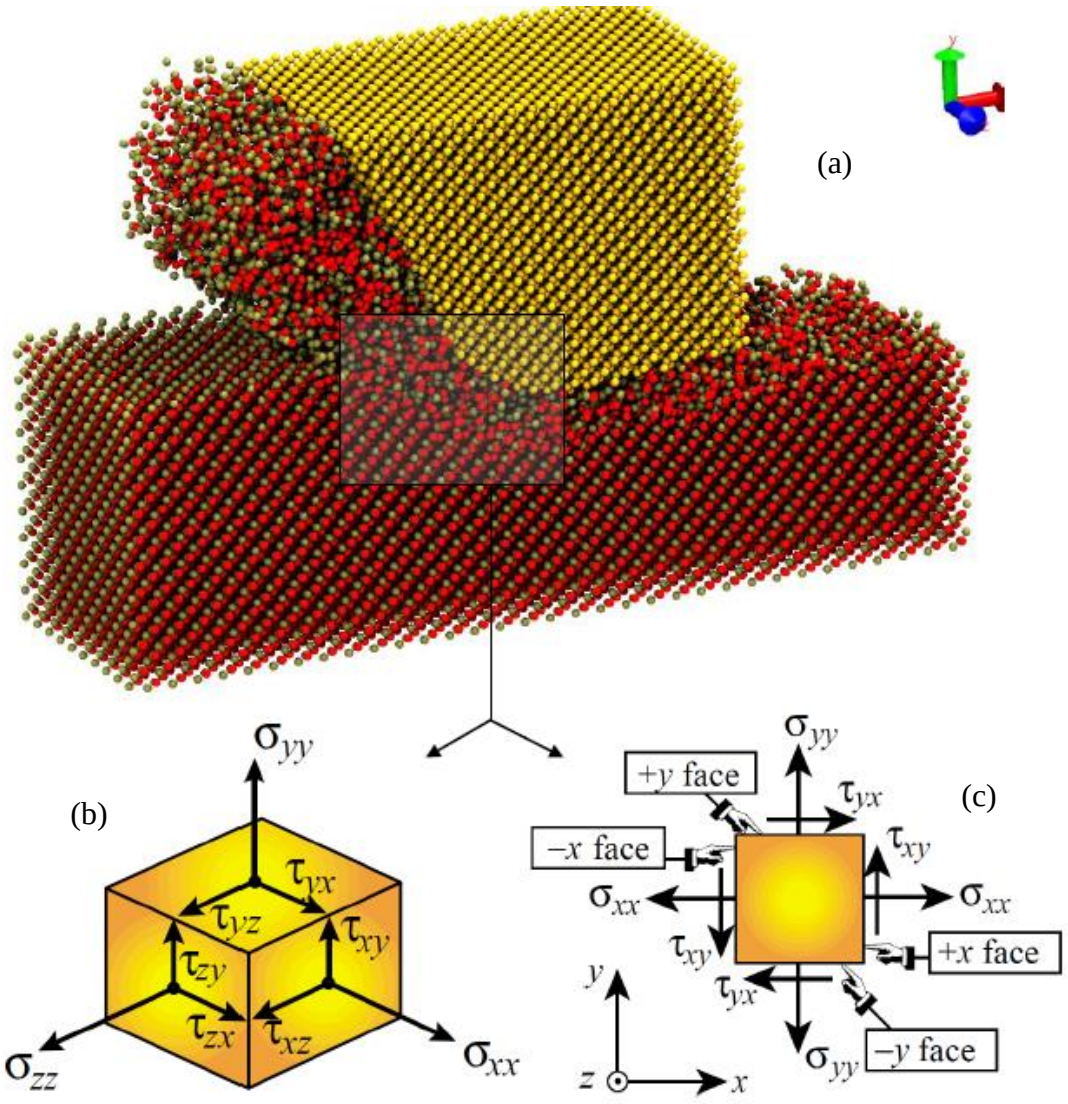

Figure 5: (a) Schematic representation of the area showing (b) 3D stress tensor in the machining zone and (c) 2D representation of the stress for a plane-stress conditions

3. Some examples of recent MDS studies

In this section, we attempt to summarize the recent state of the art studies in the field of MDS of nanometric machining of hard-brittle materials such as silicon and silicon carbide. In a nanometric machining operation, geometry of the cutting tool and anisotropy of the workpiece play a vital role and substantially influence the cutting behaviour. Hence, first, we present an insight into the effect of the aforementioned variables on the cutting behaviour of silicon and silicon carbide workpieces. In continuation, we cover MDS of hot machining and a recently-developed machining technique known as surface defect machining (SDM) in order to explore their potential capabilities for commercial implementation.

3.1.Influence of cutting tool geometry during nanometric cutting of brittle materials

It has been demonstrated that material removal at extremely fine depths of cut for certain atomic layers involves a high coefficient of friction that is dependent on the rake angle and is independent of the thrust force of the cutting tool [61]. When the uncut chip thickness approaches the size of the cutting edge radius during nanometric cutting, the rake angle of the cutting tool appears to determine both the direction and the magnitude of the resultant cutting force. Also, the use of a negative rake angle tool for single point diamond turning (SPDT) operations has become somewhat of a conventional practice for the machining of brittle materials [9, 62]. A schematic comparison of the cutting process using negative and positive rake angle tools is shown in figure 6.

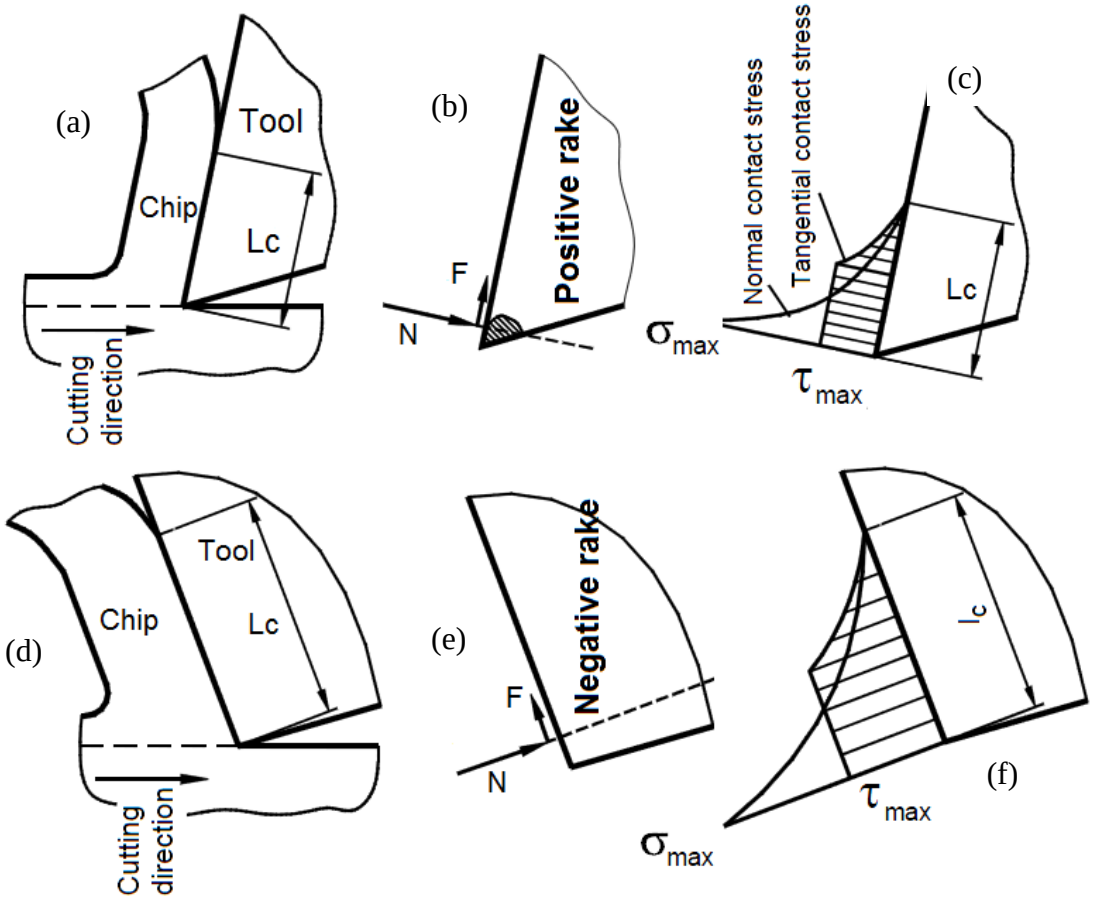

Figure 6: Difference in the force vector and stress distribution due to positive rake angle (a, b, c) and negative rake angle (d, e, f) [63] where l_c is length of contact between cutting tool and chip

It can be seen from figure 6b that the tangential force *F* acts along the wedge of the cutting tool so that the normal force acts onto the wedge face. Along these directions, the shear stress and

compressive stress on the cutting tool vary during the course of machining (figure 6c). When positive rake angles are used, the normal force exerts a bending stress on the cutting tip of the tool under which diamond, being extremely brittle, might eventually chip off. When a negative rake-angled cutting tool is used (figure 6d), this bending effect does not occur because it is replaced by compression on the cutting tool (figures 6e and 6f). Additionally, a negative rake angle cutting tool is thought to exert a hydrostatic stress state in the workpiece, which inhibits crack propagation and leads to a ductile response from brittle materials during their nanometric cutting [55, 64]. Nakasuji *et al.* [64] noted that the effect of rake angle in cutting is analogous to that of the apex angle of an indenter: low angles of approach result in relatively small hydrostatic stress fields which, in turn, enable ductile regime machining. Negative rakes of approximately -25° to -45° degrees with clearance angles of approximately 8° to 12° are recommended for improved tool life [65]. The reason for such a selection is that a high clearance angle reduces rubbing while a corresponding increase in negative rake angle provides mechanical strength to the wedge of the cutting tool [66]. It was also noted that a 0° rake angle (clearance angle of 8°) provided superior performance than a +5° or -5° rake angle for machining electro-less nickel plate die material [67]. However, this was due to the fact that when the depth of cut is smaller than the edge radius, an effective rake angle is presented by the cutting tool [68]. In such cases, a 0° rake angle tool already presents some negative rake which induces better performance than -25° or -30° rake angle tools. For hard steels, the critical value of the rake angle (the dividing line between efficient and inefficient material removal) is 0° [69]. Table II summarizes a number of key investigations of the effect of the cutting tool rake angle and clearance angle during machining of brittle materials.

Although, it is evident from table II that the rake angle and the clearance angle have a significant influence on the critical un-deformed chip thickness and the sub-surface lattice deformation layer depth. However, there is no systematic answer or model available that can be used to determine the best tool geometry for tool longevity. Komanduri *et al.* [70] used MD and a Tersoff potential function to simulate a wide range of rake angles (figure 7) to observe the mechanism of chip

formation during the nanometric cutting of silicon. They proposed a mechanism of material removal in silicon based on extrusion of plastically deformed material ahead of the tool, particularly for large negative rake angle tools, where the space available to accommodate departing chips decreases causing an increase in chip side flow. From their simulation results, they were able to explain that an increase in the negative rake angle results in a significant increase in the extent of sub-surface deformation.

Table II: Influence of rake angle on the outcome of the SPDT of brittle materials

Work material and citation	**Rake Angle**	**Clearance angle**	**Total included angle of the tool**	**Remarks/Observations**
Germanium [71]	-30°	6°	114°	Better machining conditions (large feed rate) was obtained for a -30° rake tool than a -10° and 0° rake angle tool.
Silicon [72]	-40°	5°	125°	Enabled better plastic deformation of the workpiece than that of a (-25°) rake angle tool.
Silicon [73]	-40°	10°	120°	A -40° rake angle tool provided a better ductile finished surface than a negative -20° angle rake tool.
Silicon [74] and SiC [75]	-45°	5°	130°	With an adjustable arrangement for varying rake angle, a -45° rake angle tool was found to provide better response of the workpiece for ductile-regime machining.
Silicon [76]	-25°	10°	105°	Performed better than -15° and -45° rake angle tool; however, inferior quality of gem was suspected to be the reason for poor performance of the diamond tool having -45° rake.
Silicon [77]	-25°	10°	105°	Provided a better machined surface finished in comparison to a -15° and 0° rake angle tool.
Silicon [68]	-30°	7°	113°	A rake angle between 0° and 60° was tested by keeping other parameters unchanged and a 30° rake was found superior by LLNL.
Silicon [78]	0°	Not specified	Not specified	An effective rake angle is presented by the tool when the depth of cut is smaller than the edge radius. In this condition, a 0° rake angle tool already presented some negative rake and was found to provide better finish than a -25° or -30° rake angle tool. However, a 0° rake angle tool permits reduced critical chip thickness and hence

				low material removal rate (MRR).
Silicon [79]	Varying tool rake and clearance		84°	Both tool rake angle and clearance angles were varied from -15° to -45° and from 21° to 51 ° respectively. A (-30°) rake angle tool permitted higher critical chip thickness while (-45°) angle tool enabled to reduce the micro-cracks.

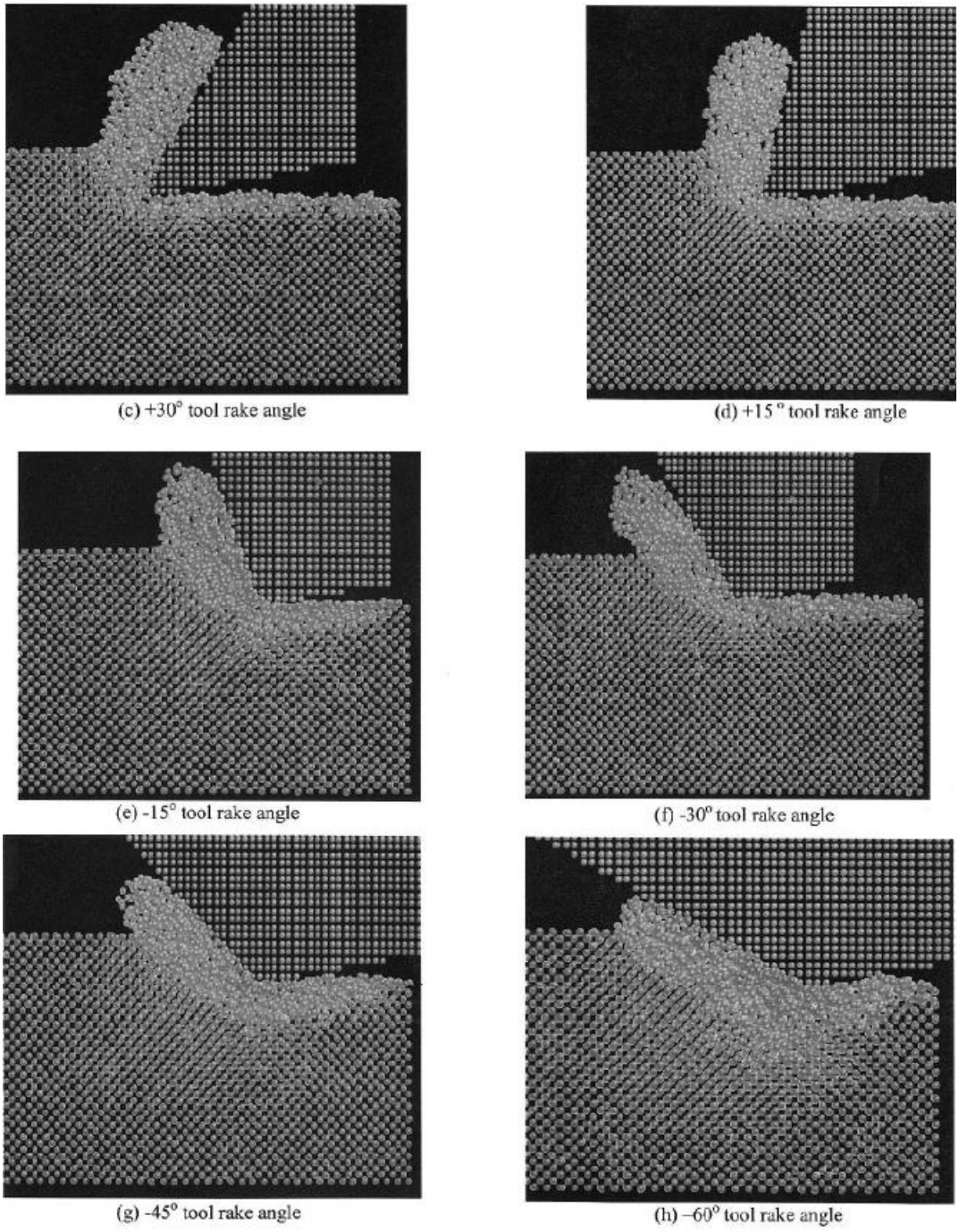

Figure 7: MD simulation of turning of silicon over a range of rake angles [70]

3.2. Influence of anisotropy of the workpiece (silicon carbide – 3C type)

Since advanced ceramics are being used in the applications historically reserved for metals, close tolerances and good surface finish are becoming increasingly important [80], especially in the field of nanotechnology. Silicon carbide (SiC) is one such non-oxide ceramic exhibiting most of these desirable engineering properties [60]. 3C-SiC is the only polytype of SiC residing in a diamond cubic lattice structure among the 250 various other polytypes of SiC recognized to date [81]. Komanduri *et al.* [65] cited Tabor, who made a recommendation regarding the selection of the cutting tools, stating that their hardness should be about 5 times that of the workpiece. In the case of SiC as a workpiece and diamond as a cutting tool, the ratio is only about 4:1, owing to the high micro hardness of SiC (about 28 GPa) compared to that of diamond (100 GPa). Experimentally, this ratio was found to reduce further to about 2:1 at relatively shallow depths of cut [82]. Hence, nanometric cutting of 3C-SiC by a single point cutting tool is expected to be surrounded by many technical challenges. Strenuous efforts are being made to find a solution to suppress the wear of cutting tools occurring during the process of nanometric cutting [19, 21, 83]. The crystal orientation of the work piece significantly affects its cutting behaviour [84] and hence a properly selected crystallographic setup could benefit both the tool life and the attainable machined surface roughness. The anisotropic variation in a material originates from the differences in the density of atoms on a particular crystal orientation and the distance between the two atoms along a specific cutting direction [85]. This in turn influences the cutting mechanics (slip occurs on the densest plane and along the shortest direction) and the nature of the plastic deformation of the workpiece material. While the knowledge of the extent of anisotropy of 3C-SiC during nanometric cutting is important, it is also important to know the variation in the Young's modulus of 3C-SiC along three major crystallographic orientations. Table III provides the estimates of the Young's modulus and Poisson's ratio obtained by applying the known analytical solutions. It is evident from table III that the maximum Young's modulus of 3C-SiC is on the (111) crystal orientation (557 GPa), while the minimum Young's modulus is on the (100) crystal orientation (314 GPa).

Table III: Direction-dependent mechanical properties in single crystal 3C-SiC

3C-SiC properties	Reference	Values
Elastic constant C_{11}	Experimental data [46]	390 GPa
Elastic constant C_{12}	Experimental data [46]	142 GPa
Elastic constant C_{44}	Experimental data [46]	256 GPa
Young's modulus (E_{100})	$C_{11} - 2\frac{C_{12}}{C_{11}+C_{12}}C_{12}$	314 GPa
Young's modulus (E_{110})	$4\frac{(C_{11}^{\ 2} + C_{12}C_{11} - 2C_{12}^{\ 2})C_{44}}{2C_{44}C_{11} + C_{11}^{\ 2} + C_{12}C_{11} - 2C_{12}^{\ 2}}$	467 GPa
Young's modulus (E_{111})	$3\frac{C_{44}(C_{11}+2C_{12})}{C_{11}+2C_{12}+C_{44}}$	557 GPa
Poisson's ratio	$\frac{C_{12}}{C_{11}+C_{12}}$	0.267
Crystal anisotropy	$\frac{E_{111}-E_{100}}{E_{111}}$	0.436

The calculated values of Young's modulus shown in table III are also verified experimentally by NASA, USA [86], and its variation proves that 3C-SiC exhibit a high degree of crystal anisotropy (up to 44%). However, the extent of this anisotropy and favourable combination of crystal orientation and cutting direction to cut 3C-SiC, and how an individual crystal setup will respond to the cutting process is not known. Figure 8 presents a schematic diagram showing the arrangement of nanometric cutting and figure 9 shows schematically the changes in symmetry, atomic density, and relationship to a number of possible cutting directions for different crystallographic planes. As evident, the arrangement of atoms, and, therefore the behaviour of the material under nanoscale cutting conditions, changes in conjunction with change in crystal setup (plane and direction) [87]. This is the reason why all the nanoscale mechanical properties, including the plastic response of brittle materials, change with respect to crystal orientations and the direction of applied force.

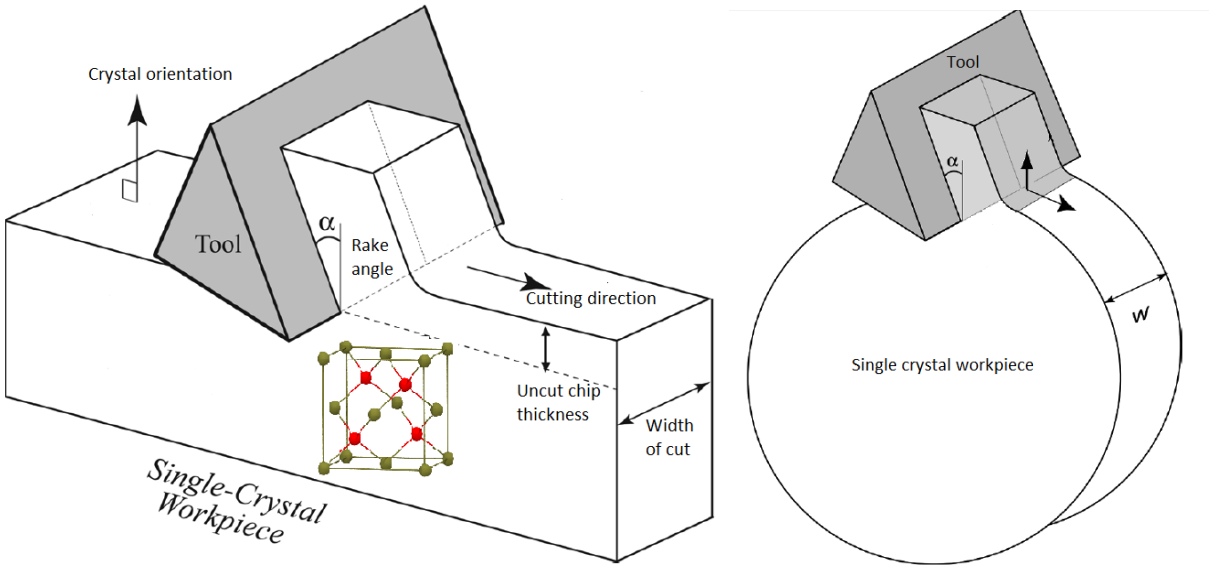

Figure 8: Schematic diagram showing the arrangement of nanometric cutting.

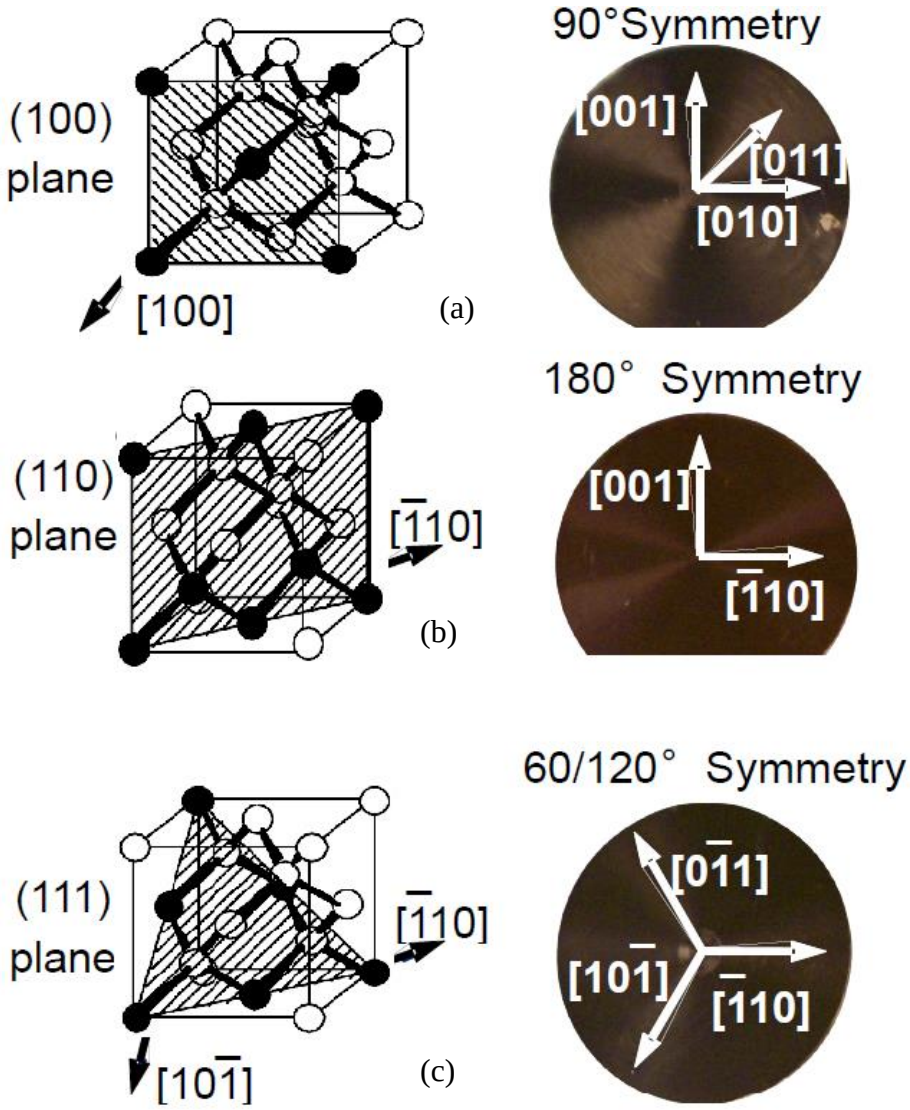

Figure 9: Schematic illustration of various crystal orientations and cutting directions in 3C-SiC on (a) (100) crystal plane, (b) (110) crystal plane and (c) (111) crystal plane

Based on figure 9, calculations were done as shown in table IV to highlight the number of atoms on a crystal plane, atomic density per unit area, minimum distance between atoms on a plane, and distance between two adjacent planes of 3C-SiC.

Table IV: Variation in the properties of 3C-SiC with respect to various crystal orientations

Orientation	Number of atoms on the plane	Atomic projection area	Atomic density per unit area	Minimum distance between the two atoms lying on the same plane	Distance between two adjacent planes
Cube (100)	$\frac{4}{4}+1=2$	a×a $=a^2$	$2/a^2$ =0.1052	a/2 = 2.18 Å	a = 4.36 Å
Dodecahedron (110)	$\frac{4}{4}+2+\frac{2}{2}=4$	$\sqrt{2}$a×a $=\sqrt{2}a^{2}$`	$4/\sqrt{2}a^2$ **=0.1488**	a/4 **= 1.09 Å**	1.707a **= 6.16 Å**
Octahedron (111)	$\frac{1}{6}\times 3+3\times\frac{1}{2}=2$	$=\frac{\sqrt{3}}{2}a^{2}$`	$4/\sqrt{3}a^2$ = 0.1215	$\sqrt{3}$a/4 =1.89 Å	0.577a = 2.514 Å

a = lattice constant of 3C-SiC = 4.36 Å.

It can be seen from table IV that the atomic density per unit area in 3C-SiC is highest on (110) crystal orientation and the distance between the two adjacent planes is farthest compared to the other two orientations. This could be expected to make (110) plane the weakest plane in comparison to the other two crystal planes. Moreover, the minimum distance between the two atoms on this orientation is shortest which makes it energetically favourable for the deformation process to occur preferentially on this crystal plane. Table V provides the details of the two sets of simulation trials performed in this work including size of the workpiece, uncut chip thickness, cutting tool, nine distinct combinations of the crystal orientations and cutting directions, and other relevant parameters.

Table V: Process variables used in the MD simulation

Details	**Simulation trial case-1**	**Simulation trial case-2**
Size of the 3C-SiC workpiece	14.262nm×4.635nm	30.1nm×11.13nm
Uncut chip thickness (d) (nm)	1.312	1.9634
Cutting edge radius (r) (nm)	2.297	1.9634
d/r ratio	0.57	1
Cutting tool rake angle	-25°	-30°
Cutting tool clearance angle	10°	
Equilibration temperature	300 Kelvin	
Cutting velocity	10 m/s	4 m/s
Potential energy function	ABOP	
Timestep	0.5 femtoseconds	
Boundary condition	PBC	
Crystal setup combinations	**Crystal orientation**	**Cutting direction**
Case-1 or crystal setup 1	(111)	<-110>
Case-2 or crystal setup 2	(111)	<-211>
Case-3 or crystal setup 3	(110)	<-110>
Case-4 or crystal setup 4	(110)	<001>
Case-5 or crystal setup 5	(001)	<-110>
Case-6 or crystal setup 6	(001)	<100>
Case-7 or crystal setup 7	(11-2)	<1-10>
Case-8 or crystal setup 8	(110)	<-11-2>
Case-9 or crystal setup 9	(1-20)	<210>

3.2.1. Variation in the cutting forces and coefficient of kinetic friction

A quantitative measure of the simulation results such as thrust forces *(F_t)*, tangential cutting forces *(F_c)*, resultant forces and coefficient of kinetic friction *(F_c/F_t)* are tabulated in table VI and plotted in figure 10 for comparison purposes. Although different *d/r* ratio, different tool rake angle, and different cutting speeds were used in the two trials, the trend of the variation and the extent of variation in the plots shown in figure 10 were eventually found to exhibit the same pattern. As is evident in the results, the thrust forces were found to be highest for the crystal setup (110) <-110> and lowest for (001) <100>. From these values, the extent of anisotropic variation in the thrust forces was observed to be around 45%. Similarly, the tangential cutting forces were found to vary by 30%, whereas the resultant force showed the extent of anisotropy of up to 37%. Contrary to the similar variation of the machining forces in both trials, friction coefficient showed significant variation. For example, a small variation in the friction anisotropy of up to 17% was noticed for high cutting speed of 10 m/sec and *d/r* ratio of 0.57 in contrast to a variation of friction anisotropy of up to 35% at a low cutting speed of 4 m/sec and *d/r* ratio of 1.

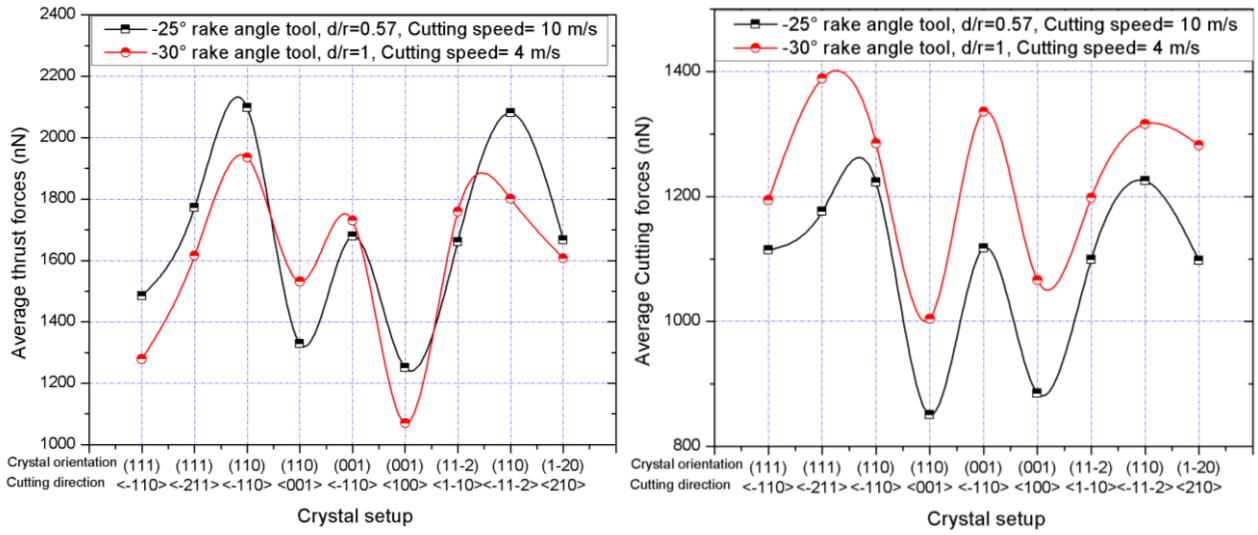

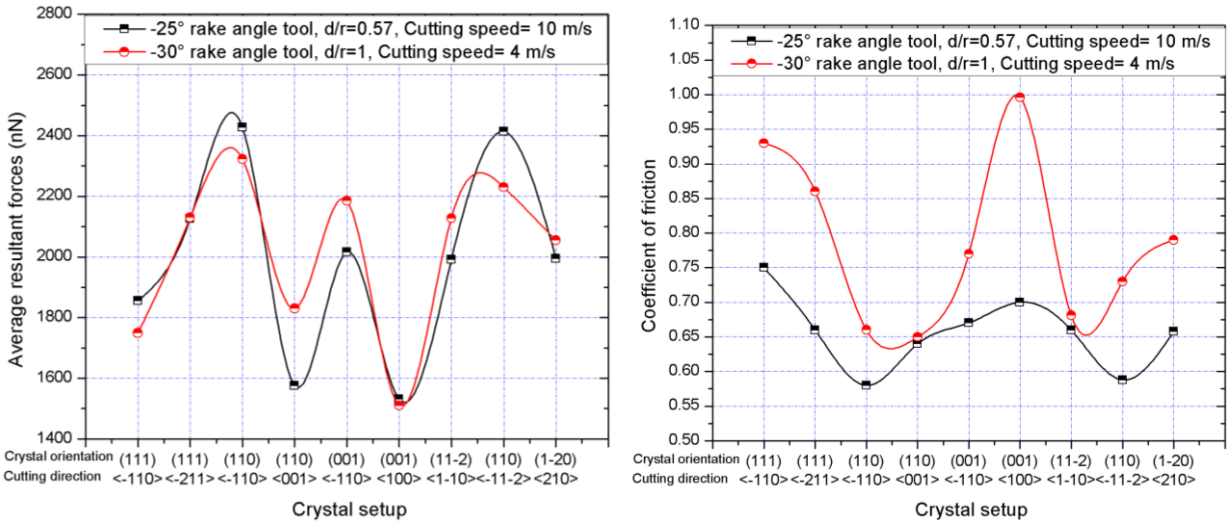

Figure 10: Variation in forces and friction coefficients (a) Average thrust forces, (b) Average cutting forces, (c) Average resultant forces, (d) Coefficient of friction

Table VI: Percentage variation in the machining forces and coefficient of kinetic friction

Crystal orientation		**111***	**111***	**110**	**110**	**001**	**001**	**11-2**	**110**	**1-20**	**% anisotropy variation**
Cutting direction		**-110**	**-211**	**-110**	**001**	**-110**	**100**	**1-10**	**-11-2**	**210**	
Average thrust force (F_t), nN	**Set 1**	1484	1772	**2098**	1328	1679	**1250**	1661	2081	1667	**40.4%**
	Set 2	1279	1616	**1936**	1531	1730	**1070**	1759	1801	1607	**44.73%**
Average cutting force (F_c), nN	**Set 1**	1114	1176	1223	**850**	1117	885	1099	**1225**	1097	**30.61%**
	Set 2	1194	1389	1285	**1004**	1316	1066	1198	**1316**	1282	**23.71%**
Average resultant force, nN	**Set 1**	1855	2126	**2428**	1576	2016	**1531**	1991	2414	1995	**36.94%**
	Set 2	1749	2130	**2323**	1830	2185	**1510**	2128	2230	2055	**35%**

Coefficient of kinetic friction, (F_c/F_t)	**Set 1**	0.75	0.66	**0.58**	0.64	0.67	**0.7**	0.66	0.588	0.658	**17.14%**
	Set 2	0.93	0.86	**0.65**	0.65	0.77	**0.996**	0.681	0.73	0.79	**34.73%**

***Mechanism of material removal on (111) plane was cleavage/fracture dominant, that is why cutting forces dropped during the occurrence of fracture. Consequently, the average forces appear to be lower here. Therefore, machining outcomes on (111) crystal orientation in its current format cannot be considered to quantify the anisotropy.**

3.2.2. Variation in the machining temperature and machining stresses

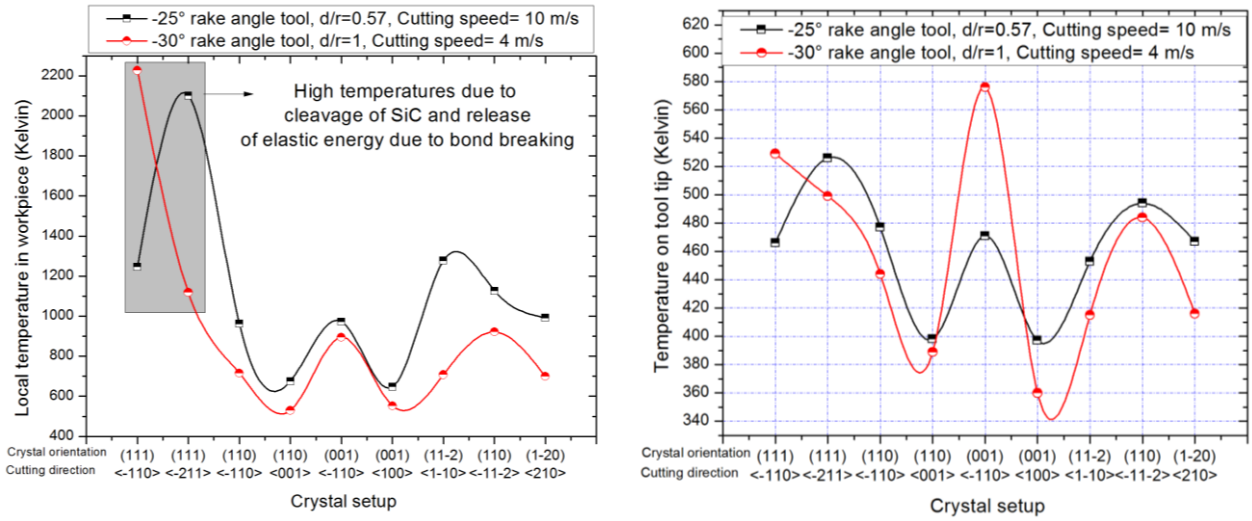

(a) (b)

Figure 11: Variation in the temperature (a) in the machining zone of the workpiece and (b) on the tool tip

Figure 11 and table VII show the variation in the temperature in the machining zone of SiC with respect to change in orientations. Figure 11a shows the variation in the peak temperature of the workpiece with respect to change in crystal setup and figure 11b shows the variation in the average of the peak temperature of the atoms in the cutting edge radius of the tool. It can be seen from a comparison of figure 11a and figure 11b that the trend of plot in both simulation trials is quite similar. It is further evident from figure 11a that the local temperature in the workpiece went up to 2000-2200 K when the cutting was performed on the (111) crystal orientation. It is noteworthy to refer to the earlier discussions on the occurrence of cleavage on (111) crystal orientation. An

occurrence of cleavage releases a tremendous amount of elastic energy in the form of heat, which gets transmitted to both the workpiece and to the cutting tool. Consequently, the local temperature of the workpiece in this particular case increases to about 2200 K while the cutting tool edge temperature increases to around 520 K during cutting on the (111) orientation. Interestingly, materials exhibiting a large ratio of covalent bonding do not get affected at elevated temperatures as much as ionic bonded materials in terms of their mechanical properties, especially the ease with which they could mechanically be deformed [80]. This is also the reason why SiC exhibits lower coefficient of thermal expansion and high thermal conductivity. The ratio of covalent to ionic bonding in SiC is about 1:9, which indicates the fact that it is the concentrated shear rather than the adiabatic shear, that drives the ductility in SiC during its nanometric cutting [87]. Along the easy cutting directions, the temperature increase in the workpiece was only up to 600K. In addition, during cutting on easy cutting directions, i.e. Case-4 and Case-6 in table VII, the lowest temperature on the cutting tool was observed, whereas Case- 3, Case-5, and Case-8 showed a somewhat higher temperature on the cutting tool and workpiece.

Table VII: Percentage variation in temperature and stresses

Crystal orientation		**111***	**111***	**110**	**110**	**001**	**001**	**11-2**	**110**	**1-20**
Cutting direction		**-110**	**-211**	**-110**	**001**	**-110**	**100**	**1-10**	**-11-2**	**210**
von Mises stress in the machining zone of the workpiece (GPa)	**Set 1**	100	112^{+}	110	**65**	78	85	89	110^{+}	94
	Set 2	110^{+}	96	101	**58**	90	74	62	86	77
von Mises stress on the cutting edge of the diamond tool	**Set 1**	343	350	380	**322**	343	**300**	322	354	355
	Set 2	400	419	386	**386**	412	**325**	337	380	388

Average temperature in the machining zone of the workpiece (Kelvin)	**Set 1**	1247	2102	962	**675**	973	**648**	1277	1127	992
	Set 2	2227	1119	715	**529**	896	**553**	708	921	699
Average temperature on the cutting edge of the tool (Kelvin)	**Set 1**	466	526	477	**398**	471	**397**	453	494	467
	Set 2	529	499	444	**389**	576	**360**	415	484	416

*** Mechanism of material removal on (111) plane was cleavage/fracture dominant which is the reason that the cleavage energy gets transformed to cutting heat and is apparent in the results.**

$^{+}$ reflects stress concentration responsible for the occurrence of cleavage

Figure 12 in conjunction with table VII shows the variation in the von Mises stresses in the machining zone. A high magnitude of von Mises stress of up to 112 GPa can be seen when cutting was performed on (111) orientation unlike Case- 4 (an easy cutting direction) where this magnitude was only a maximum of 58 GPa. Thus, it appears that it is the high stress concentration that is responsible for the occurrence of cleavage on (111) crystal orientation. Knowledge of the stress state on the cutting tool is very promising information. In this context, stresses that acted on the cutting tool during nanometric cutting of 3C-SiC on crystal setups (110) <001> and (001) <100> were found minimum and similar in magnitude, suggesting that these two setups should be the preferred orientations for cutting of 3C-SiC. In common with 3C-SiC, these two crystal setups are once again known to be soft cutting directions for easy material removal in diamond.

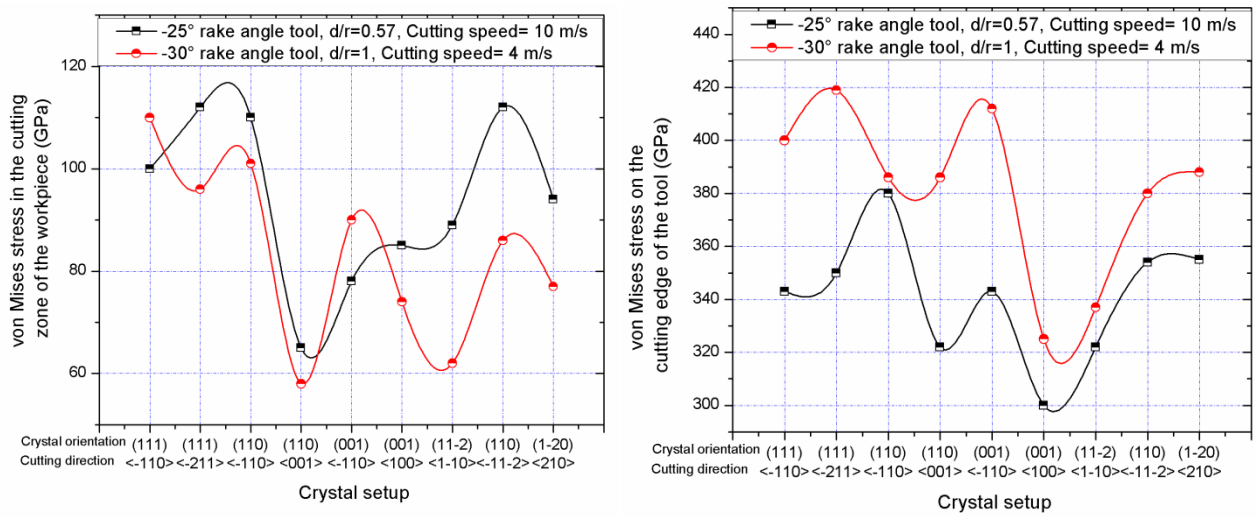

(a) (b)

Figure 12: Variation in the von Mises stress on different crystal setups of (a) workpiece and (b) on the tip of the cutting tool

An overall analysis of the machining stresses, temperature in the machining zone and cutting forces obtained from the MD simulation shown above suggest that the amenability of 3C-SiC of being cut in particular crystal setups can be tabulated as shown in table VIII:

Table VIII: Influence of anisotropy on the cutting behaviour of 3C-SiC found from the MDS

Crystallographic planes of 3C-SiC	Least amenable cutting directions	More amenable cutting directions
Cube (001)	<-110>	<100>
Dodecahedron (110)	<-11-2>	<001>
Octahedron (111)	<-211>	<-110>

The anecdote of this MD simulation study (table VIII) is that cutting of 3C-SiC is preferred on the <100> direction on the cubic plane, <001> direction on the Dodec plane and in the <-110> direction on the octahedron plane. These results, along with the previous simulation case study results demonstrate the value of Molecular Dynamics simulation to understand and improve nanometric machining processes.

3.3. Surface defect machining and hot machining of nanocrystalline silicon carbide

In this section, the efficiency of the "surface defect machining" (SDM) and hot machining has been

assessed by using MDS. SDM is a recently proposed method of machining that aims to obtain better quality of a machined product at lower costs. This method utilizes pre-defined and machined surface defects on the workpiece to ease material removal. The central idea of this method is to generate surface defects in the form of a series of holes on the top surface of the workpiece prior to the actual machining operation (figure 13). The presence of these defects changes the homogeneity and thus reduces the structural strength of the workpiece which in turn aids to lower the cutting resistance during machining. Recent experimental trials [13] and numerical simulations [12] on hard steels have shown some very interesting salient features of the SDM method such as lower machining forces, reduction in overall temperature in the cutting zone, reduced machining stresses and increased chip flow velocity. In the following paragraphs, the applicability of SDM for machining silicon carbide is explored.

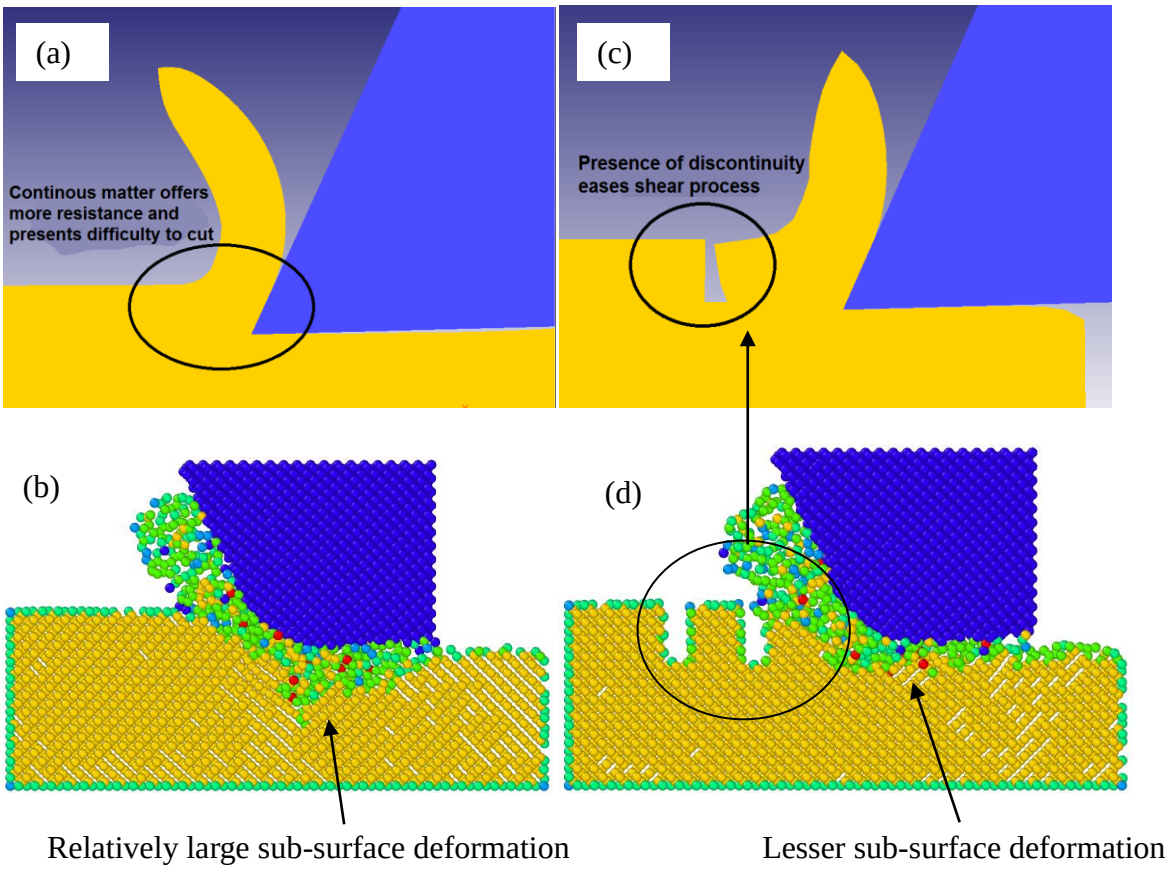

Figure 13: Schematic diagram indicating the differences between the mode of deformation during conventional machining (a) observed using FEA and (b) observed using MD simulation and the mechanics of chip formation during SDM (c) observed using FEA and (d) observed using MD simulation respectively

This section details the results of a case study made on machining of beta silicon carbide (3C-SiC), but this method is versatile and can readily be applied to other engineering materials which are not readily machinable through conventional approaches e.g. titanium [88], silicon [89], nickel [90], pretentious low carbon ferrous alloys [91-92], various polytypes of silicon carbide [75, 93], silicon nitride [94] and Al-SiC_p metal matrix composites [95] where rapid tool wear and consequent deterioration to the quality of surface remains a major concern till date. Researchers have also investigated preferential heating and thermal softening of the workpiece by a laser device prior to machining. While this approach has shown promise [96-98], its adverse undesirable effects such as the lack of control on laser power, sub-surface deformation and transfer of heat to the cutting tool has impeded its commercial realization. Overall, the key question explored in this section is this: Can SiC be machined using SDM method so that the machined surface exhibits improved quality? The results from SDM are compared with (i) Hot machining at 1200 K, a temperature where SiC has been reported to gain significant plasticity [99] and (ii) Normal machining at 300 K, in order to test the robustnesss of the proposed method. To describe the interatomic interaction of the atoms, the ABOP [46] potential energy function was employed since it is the only three-body potential energy function developed till date that does not suppress the mechanism of cleavage in 3C-SiC [23]. A comprehensive description along with the key parameters of the ABOP potential function is provided elsewhere [46] in its respective reference and for the purpose of brevity they are not repeated here in this section. Table IX lists the computational parameters, details of the workpiece, uncut chip thickness, details of the cutting tool and other relevant parameters used in this study. The criterion for the selection of these parameters was chosen so that these can readily be linked with the previously performed studies [21, 100].

Table IX: Process variables used for performing the MD simulation

Workpiece material	Number of atoms in the workpiece	Number of atoms in the diamond cutting tool
3C-SiC without holes (14.26 nm ×	28170	21192

4.6345 nm × 4.278 nm)		
3C-SiC with surface defects (holes) 14.26 nm × 4.6345 nm × 4.278 nm)	27782	21192
Equilibrium lattice parameters for 3C-SiC:		a= 4.36 Å; α = β= γ= 90°
Details of surface defects (holes): Total number Diameter of each hole Depth of each hole		 7 0.713 nm 1.426 nm
Crystal orientation of the workpiece		(010)
Crystal orientation of diamond tool		Cubic
Cutting direction		<100>
Cutting edge radius (nm)		2.297
Uncut chip thickness / in-feed (nm)		1.3126
Cutting tool rake and clearance angle		-25° and 10°
Equilibration temperature		300 Kelvin
Hot machining temperature		1200 Kelvin
Cutting velocity		10 m/s
Timestep		0.5 femto seconds

A snapshot from the MD simulation after equilibration process (with surface defects in the 3C-SiC workpiece) is shown in Figure 14 where the red and grey colours‡ correspond to silicon and carbon atoms in the workpiece and yellow colour represents carbon atoms within the diamond cutting tool respectively.

‡ Readers are referred to the web based version of this work to interpret the correct colour legends.

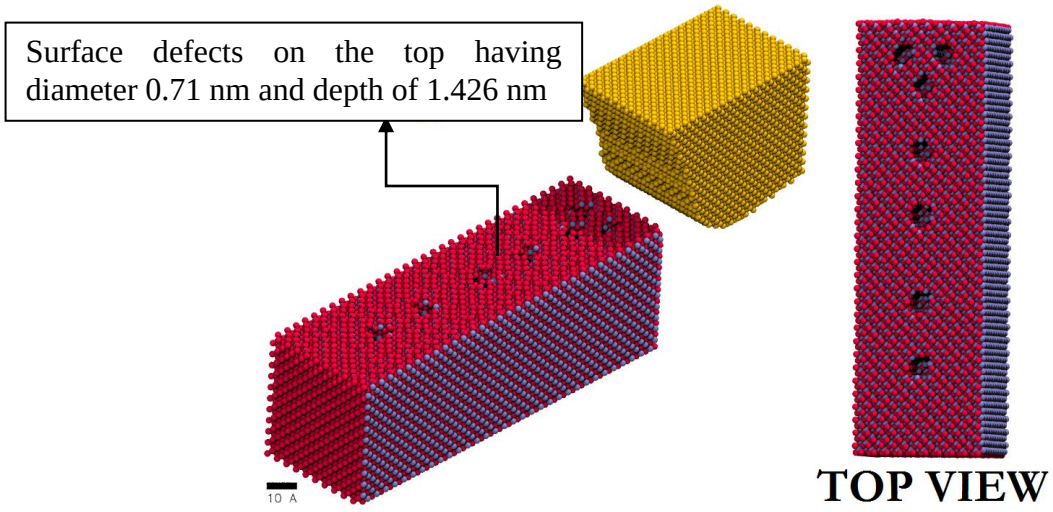

Figure 14: Snapshot from MD simulation for 3C-SiC specimen with surface defects on top.

An important constraint of MD simulation studies is that they are computationally expensive, and therefore use of high cutting speeds is frequent in MD simulation studies e.g. 500-2500 m/sec cutting speed was used by Belak *et al.* [3, 101] and Komanduri *et al.* [61, 102], 150-400 m/sec was used by Wang *et al.* [103] and Liang *et al.* [104], 70-100 m/sec was used by Noreyan *et al.* [105-106], Rentsch *et al.* [107] and Goel *et al.* [83, 100]. Although, these investigations have been successful to capture key insights of the cutting process but in the current investigation, high cutting speed could have affected the sensitivity of the results, particularly when cutting of the same configuration is to be compared at 300 K and 1200 K. Therefore, a more realistic cutting speed, 10 m/sec, was employed to perform the MD simulations that are presented here. This is accomplished using parallel computing through MPI interface. The calculation time for each simulation case depends on the model size, cutting speed, cutting distance and the number of CPUs used.

3.3.1. Evolution of the machining forces

A comparison of the evolution of machining forces (F_c and F_t) obtained from the MD simulation is shown in Figure 15 and Figure 16 for all the three cases studied (i) Nanometric cutting at 300K, (ii) Nanometric cutting at 1200K, and (iii) Cutting with surface defect machining at 300 K.

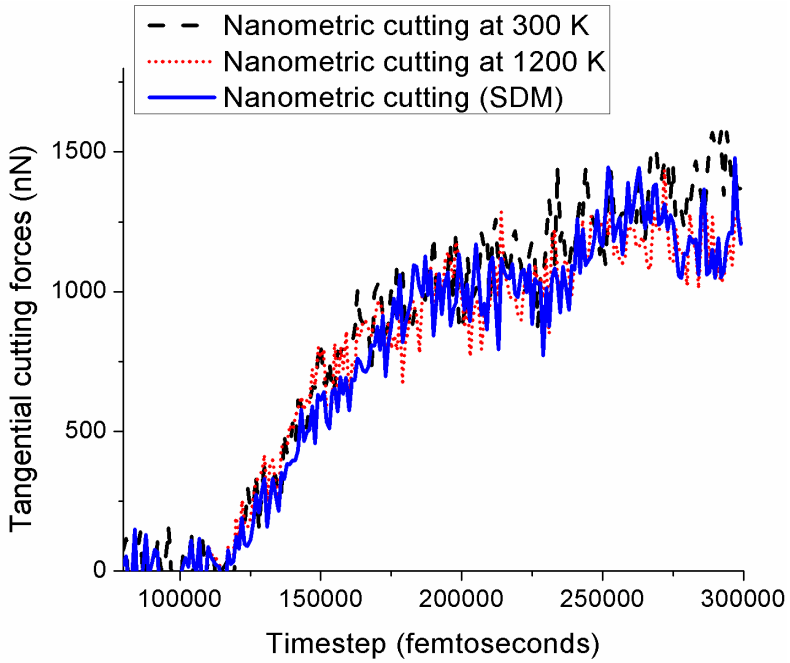

Figure 15: Tangential cutting forces during nanometric cutting of 3C-SiC in three cases

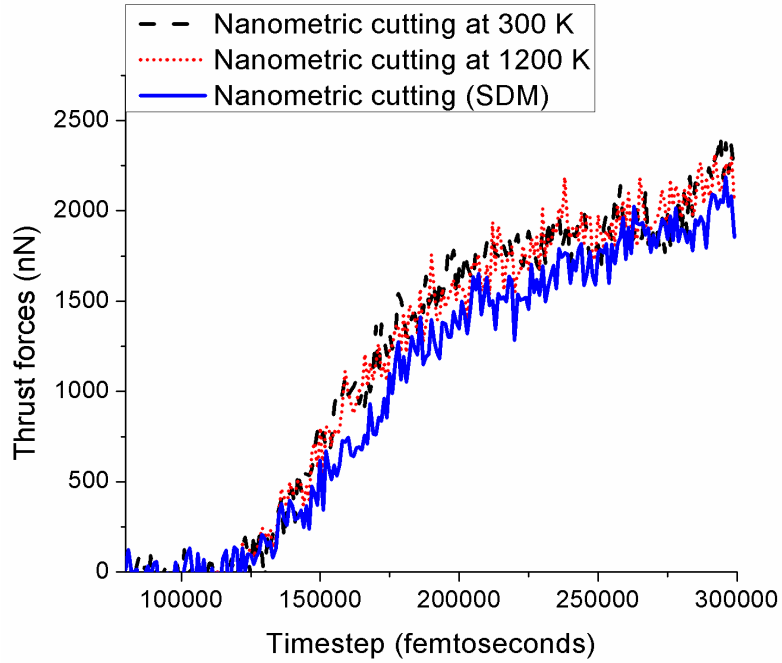

Figure 16: Thrust forces during nanometric cutting of 3C-SiC in three cases

It can be seen from Figure 15 and Figure 16 that the magnitudes of both forces are significantly higher during conventional nanometric cutting performed at 300K. However, during nanometric cutting at elevated temperature of 1200K, both tangential cutting force and thrust force reduce, albeit, to a lesser extent. On the other hand, a noticeable reduction, especially in thrust forces, can

be seen during nanometric cutting in the case of SDM. It can be noted here that the extent of reduction in cutting force during SDM will depend on various parameters such as the number of holes, dimensions of holes, interspacing between holes, and shape of holes. However, since the reduction in the cutting force is of intermittent nature, the cutting forces and thus stresses on the cutting tool would be relieved as soon as the hole is encountered by the cutting tool. Table X summarizes various results obtained from the simulation under different machining conditions i.e. average cutting force, friction coefficient and resultant cutting force.

Table X: Comparison of cutting forces and friction coefficient during cutting of 3C-SiC

S.N.	Machining condition	Average tangential cutting force (F_c)	Average thrust force (F_t)	Average resultant force ($\sqrt{(F_t^2+F_c^2)}$)	Average friction coefficient (F_c / F_t)
1	Normal machining (300K)	835 nN	1185 nN	1449.64 nN	0.7046
2	Hot machining (1200K)	762 nN	1177 nN	1402.13 nN	0.6474
3	Surface defect machining (300K)	751 nN	1038 nN	1281.19 nN	0.7235

The data in Table X shows that the resultant cutting force reduces from a value of 1449.64 nN to 1402.13 nN when the machining was done at 1200K instead of at 300K, signifying a reduction in the cutting resistance of 3C-SiC by 3.27% at 1200K. However, the extent of this reduction is higher during the surface defect machining process as the resultant forces drops to 1281.19 nN i.e. a significant reduction of 11.62% compared to normal nanometric cutting at 300K. It is very interesting to note here that while the cutting force showed a reducing trend, similar trend is not visible for the coefficient of friction. Compared to the nanometric cutting results at 300 K, the

coefficient of friction reduces by 8.11% when the cutting was performed at 1200 K. On the contrary, surface defect machining causes an increase in the friction coefficient by 2.68%. This suggests that a different mechanism of chip formation is associated with the proposed SDM method which will be discussed here now.

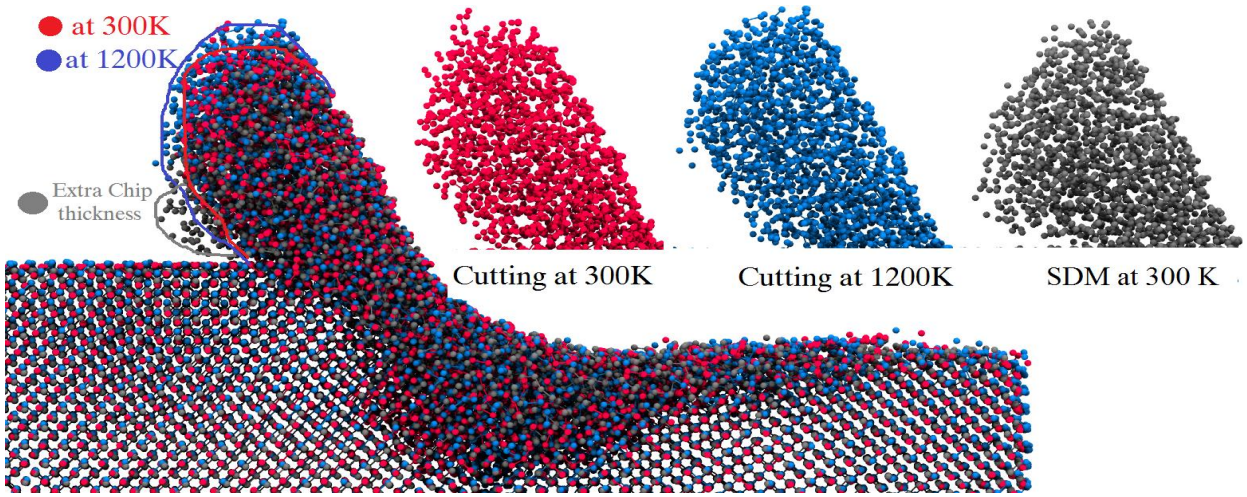

Figure 17: Chip morphology of 3C-SiC while cutting the workpiece after tool advances to 8.3 nm (see online coloured version for interpreting correct colours)

Figure 17 shows a superimposed image and a comparison of the chip morphology in all the three cases investigated. On comparing nanometric cutting at 1200K with conventional nanometric cutting at 300K, it can be seen that the curliness of the chip has seemingly increased which is plausible due to the increased plasticity of SiC at high temperature of 1200K. However, the shear plane angle remained unchanged, which is not the case with SDM. In the case of SDM, the cut chip thickness has increased and thus the shear plane angle has decreased. This was verified using the following equation:

$$\tan\phi = \frac{r\cos\alpha}{1 - r\sin\alpha} \tag{5}$$

where φ is shear plane angle, α is rake angle and *r* is the ratio of uncut and cut chip thicknesses.

Table XI: Comparison of chip morphology and shear angle during machining of 3C-SiC under different machining conditions

S.N.	Machining condition	Ratio of uncut chip thickness to cut chip thickness (r)	Shear plane angle(φ)
1	300 K	0.525	21.28°
2	1200 K	0.525	21.28°
3	SDM at 300 K	0.505	20.66°

Table XI shows a decrease in shear plane angle from a value of 21.28° to 20.66° using SDM process compared to nanometric cutting at 300K. A decrease in the value of shear plane angle under the same machining parameters shows the dominance of tangential cutting force over thrust force which justifies the enhanced cutting action of the tool. This corroborates to the increased force ratio as seen earlier in Table X during the case of SDM suggesting the dominance of tangential cutting force to be the reason of the increase in friction coefficient (which improves the cutting action).

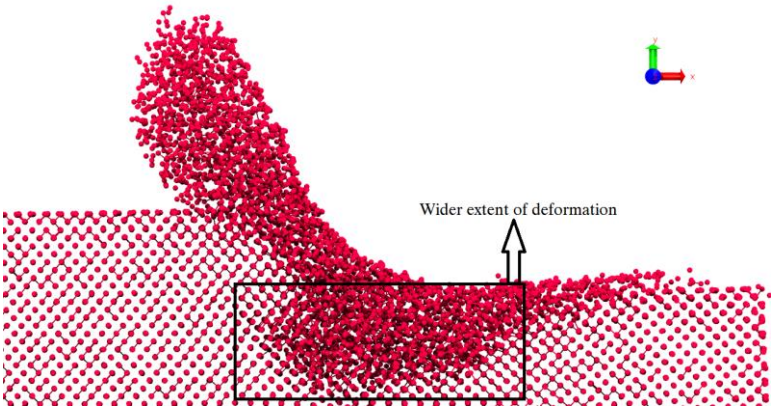

(a) Conventional cutting at 300K

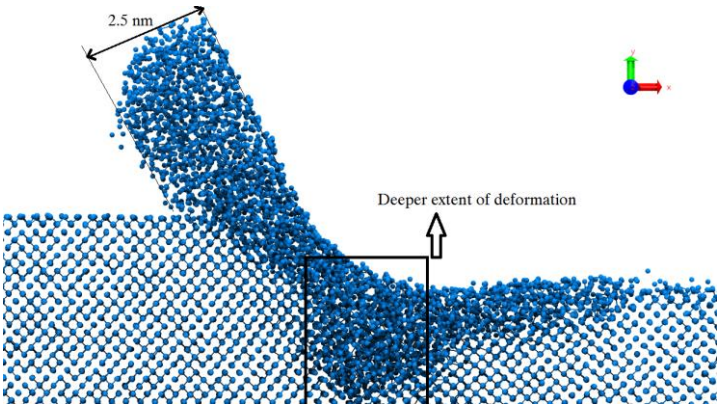

(b) Cutting at 1200K

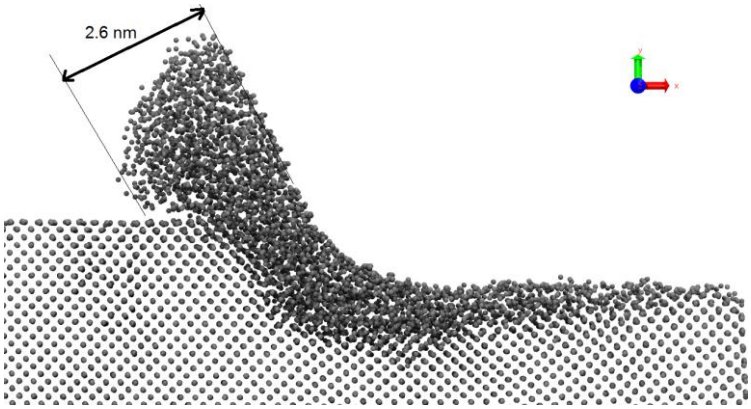

(c) Cutting at 300K with SDM process

Figure 18: Sub-surface crystal lattice deformation of 3C-SiC after tool advances to 8.3 nm

Figure 18 shows the measure of the cut chip thickness and highlights the variation in the sub-surface crystal deformation lattice layer depth. It is interesting to note that the sub-surface crystal deformation lattice layer becomes wider while cutting at 300K while it becomes a little deeper while cutting at 1200K. Moreover, the extent of the deformation of crystal layer underneath the finished surface is more pronounced in both these cases compared to that in the SDM operation. It can be postulated that high temperature weakens the bonding forces between the atoms and hence, the atoms could easily be deformed without having much influence on the neighbour atoms. Therefore, the deformation did not become wider and remained concentrated under the wake of the tool under the influence of high deviatoric stresses. Contrarily, SDM process shows minimal sub-surface deformation. The waviness of the finished surface also seems to have decreased during SDM. The defects generated manually for the purpose of SDM significantly weaken the material

locally, which in turn reduces the bonding strength of the atoms in the area of uncut chip thickness without disturbing the sub-surface. Also, a discontinuity in the material and the consequent lack of resistance to the deformation of the atoms by the adjacent atoms makes the shearing process more preferential. Eventually, the material removal is facilitated by local shearing of the material which is promoted further by stress concentration. This is compounded by the fact that the cutting tool is relieved from high cutting forces intermittently and this results in minimal sub-surface damage.

3.3.2. Temperature and stress variation during SDM

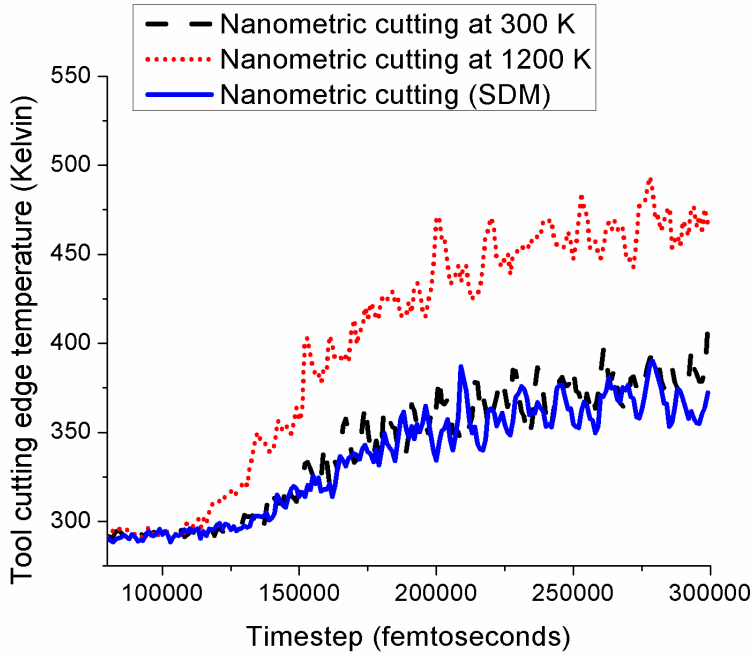

Figure 19: Variation in the temperature of the cutting edge during nanometric cutting of 3C-SiC

A comparison of the evolution of the cutting temperature on the tool cutting edge in all the three cases is shown in figure 19 over the cutting length of 9.35 nm. From this graph, a high temperature of 480 K on the tool cutting edge is evident during nanometric cutting at 1200 K. At higher temperature, graphitization of diamond becomes inevitable [100]. The transfer of heat from the bulk of the workpiece to the cutting tool may thus compromise the life of diamond tools [83]. On the contrary, the temperature on the tool cutting edge was observed to be much lower during SDM. This shows that the SDM cutting process could potentially release the cutting tool from high cutting

loads and high temperature intermittently which provides longevity to the tool life.

It will be interesting to analyse the variation in the stresses on the cutting tool during SDM and conventional nanometric cutting to understand the process differences in detail. Figure 20 and Figure 21 show the evolution of the von Mises stress and shear stress acting on the cutting tool, respectively over the cutting length of 9.35 nm.

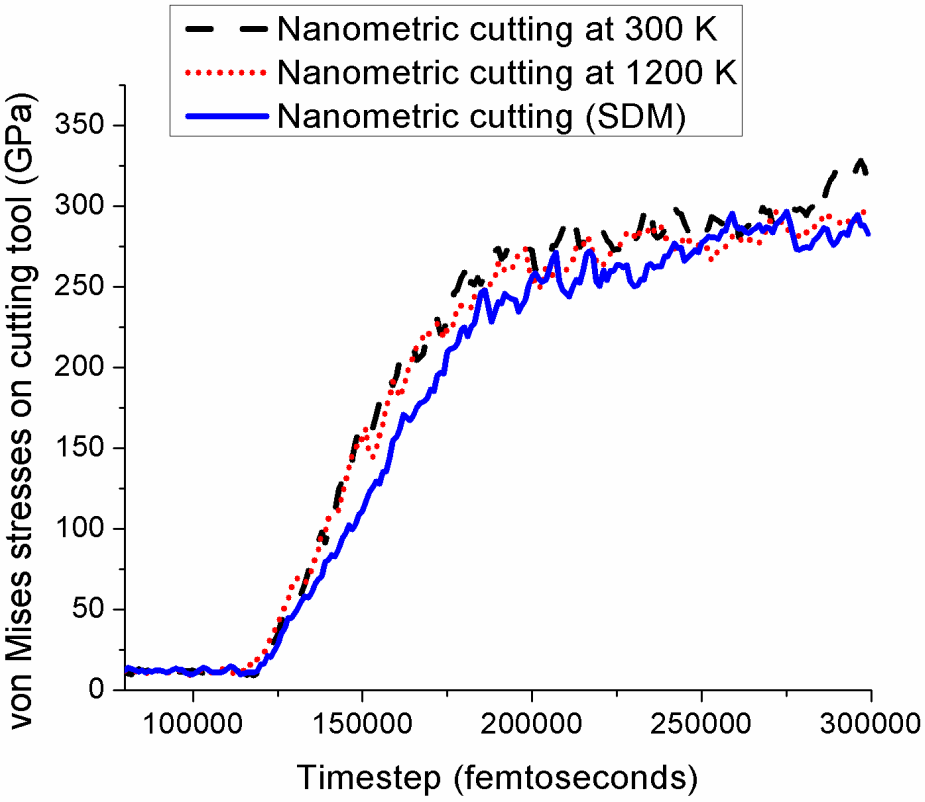

Figure 20: Variation in von Mises stress acting on the tool during nanometric cutting of 3C-SiC.

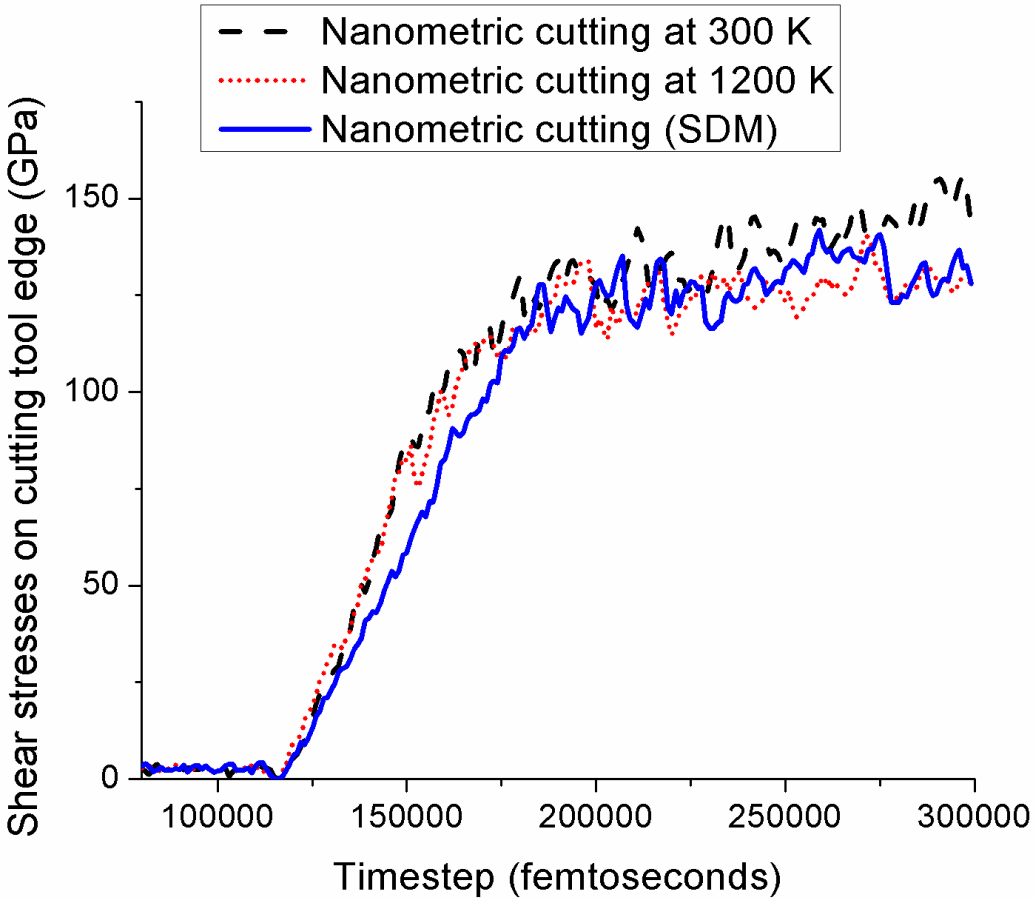

Figure 21: Variation in shear stress acting on the tool during nanometric cutting of 3C-SiC.

From figure 20 and figure 21, it appears that in all the three cases, the diamond tool cutting edge has undergone a high magnitude of von Mises stress and shear stress during nanometric cutting of 3C-SiC. This can be attributed to the high hardness of 3C-SiC, which offers tremendous cutting resistance in comparison to other relatively softer brittle materials. A high magnitude of von Mises stress of up to 250 GPa having a component of shear stress to the order of 125 GPa is certainly unfavourable for the life of the diamond cutting tool —the ideal strength for diamond prior to graphitization has been reported to be around 95 GPa [108]. The stress state in all the cases suggests that graphitization of diamond tool during nanometric cutting of 3C-SiC would be inevitable owing to the high hardness of 3C-SiC. However, SDM seems to have aided to reduce the stresses on the cutting edge to some extent in comparison to conventional approach of nanometric cutting and hot machining at 1200K.

In summary this section has presented a case study on the nanometric machining of silicon and

silicon carbide using MD simulations. To begin with, the geometry of the cutting tool, particularly the rake angle, has a marked impact in dictating the plasticity from hard-brittle materials. It was also demonstrated that the silicon carbide exhibits strong anisotropy in its ease of deformation and rigorous analysis shows that the combinations of either (110) <001> or (001) <100> crystal orientations and cutting directions are favourable to cut 3C-SiC. In an effort to overcome the problems of tool wear, a new method namely, surface defect machining has been presented which turns out to be advantageous because both cutting as well as polishing mechanisms are realised, improving surface roughness. Further investigations may be directed to realise the optimum shapes of surface defects, pathways to generate such defects in a controlled environment and net saving in energy and cost. Such understanding is only possible through Molecular Dynamics simulation and these results again demonstrate the value of using Molecular Dynamics to understand novel machining processes for the most challenging materials.

4. Concluding Remarks

Molecular Dynamics Simulations (MDS) are constantly being used to make important contributions to our fundamental understanding of material behaviour, at the atomic scale, for a variety of thermodynamic processes. This chapter shows that molecular dynamics simulation is a robust numerical analysis tool in addressing a range of complex nanofinishing (machining) problems that are otherwise difficult or impossible to understand using other methods. For example the mechanism of nanometric cutting of silicon carbide is influenced by a number of variables such as machine tool performance, machining conditions, material properties, and cutting tool performance (material microstructure and physical geometry of the contact) and all these variables cannot be monitored online through experimental examination. However, these could suitably be studied using an advanced simulation based approach such as MDS. This chapter details how MD simulation can be used as a research and commercial tool to understand key issues of ultra precision manufacturing research problems and a specific case was addressed by studying diamond machining of silicon carbide. While this is appreciable, there are a lot of challenges and

opportunities in this fertile area. For example, the world of MD simulations is dependent on present day computers and the accuracy and reliability of potential energy functions [109]. This presents a limitation: Real-world scale simulation models are yet to be developed. The simulated length and timescales are far shorter than the experimental ones which couples further with the fact that contact loading simulations are typically done in the speed range of a few hundreds of m/sec against the experimental speed of typically about 1 m/sec [17]. Consequently, MD simulations suffer from the spurious effects of high cutting speeds and the accuracy of the simulation results has yet to be fully explored. The development of user-friendly software could help facilitate molecular dynamics as an integral part of computer-aided design and manufacturing to tackle a range of machining problems from all perspectives, including materials science (phase of the material formed due to the sub-surface deformation layer), electronics and optics (properties of the finished machined surface due to the metallurgical transformation in comparison to the bulk material), and mechanical engineering (extent of residual stresses in the machined component) [110]. Overall, this chapter provided key information concerning diamond machining of SiC which is classed as hard, brittle material. From the analysis presented in the earlier sections, MD simulation has helped in understanding the effects of crystal anisotropy in nanometric cutting of 3C-SiC by revealing the atomic-level deformation mechanisms for different crystal orientations and cutting directions. In addition to this, the MD simulation revealed that the material removal mechanism on the (111) surface of 3C-SiC (akin to diamond) is dominated by cleavage. These understandings led to the development of a new approach named the “surface defect machining” method which has the potential to be more effective to implement than ductile mode micro laser assisted machining or conventional nanometric cutting.

Acknowledgments:

The authors acknowledge funding support from the International Research Fellowship account of Queen’s University, Belfast in undertaking this work. The authors would also like to acknowledge the use of HPC service of STFC Hartree Centre.

References:

1. Alder, B.J. and T.E. Wainwright, J. Chem. Phys., 1957. **1208**(27).
2. Brinksmeier, E. and O. Riemer, International Journal of Machine Tools and Manufacture, 1998. **38**(5–6): p. 699-705.
3. Belak, J.F. and I.F. Stowers, Proceedings of American Society Precision Engineering Annual conference, 1990: p. 76-79.
4. Landman, U., et al., Science, 1990. **248**(4954): p. 454-461.
5. Ikawa, et al., Nanotechnology, 1992. **1**(3): p. 6-9.
6. Voter, A.F. and J.D. Kress. *Atomistic Simulation of Diamond-Tip Machining of Nanoscale Features*. in *Principles of Cutting Mechanics: Applications of Ultra-Precision Machining and Grinding, 1993 Spring Topical Meeting* 1993. Tucson, AZ, USA: ASPE Proceedings.
7. Inamura, T., et al., CIRP Annals - Manufacturing Technology, 1997. **46**(1): p. 31-34.
8. Rentsch, R. *Influence of Crystal Orientation on the Nanomeric Cutting Process*. in *Proceedings of the First International Euspen Conference*. 1999. Bremen, Germany,.
9. Komanduri, R., N. Chandrasekaran, and L.M. Raff, Wear, 1998. **219**(1): p. 84-97.
10. Goel, S., et al., Materials Science and Engineering: A, 2015. **627**(0): p. 249-261.
11. Goel, S., et al., Journal of Manufacturing Science and Engineering, 2014. **136**(2): p. 021015.
12. Rashid, W.B., et al., Wear, 2013. **302**(1–2): p. 1124-1135.
13. Rashid, W.B., et al., Proceedings of the Institution of Mechanical Engineers, Part B: Journal of Engineering Manufacture, 2013. **227**(2): p. 338-342.
14. Goel, S., et al., Computational Materials Science, 2014. **84**(0): p. 163-174.
15. Faisal, N.H., et al., Surface and Coatings Technology, 2014. **242**(0): p. 42-53.
16. Goel, S., A. Agrawal, and N.H. Faisal, Wear, 2014. **315**(1-2): p. 38-41.
17. Goel, S., et al., Journal of Physics D: Applied Physics, 2014. **47**(27): p. 275304.
18. Goel, S., et al., Materials Science and Engineering: A, 2014. **597**(0): p. 331-341.
19. Goel, S., et al., International Journal of Machine Tools and Manufacture, 2013. **65**(February): p. 15-21.
20. Goel, S., X. Luo, and R.L. Reuben Applied Physics Letters, 2012. **100**(23): p. 231902.
21. Goel, S., X. Luo, and R.L. Reuben, Tribology International, 2013. **57**(0): p. 272-281.
22. Goel, S., et al., Beilstein Journal of Nanotechnology, 2012. **3**: p. 586-588.
23. Goel, S., et al., Modelling and Simulation in Materials Science and Engineering, 2013. **21**(6): p. 065004.
24. Goel, S., Journal of Physics D: Applied Physics, 2014. **47**(24): p. 243001.
25. Goel, S., et al., International Journal of Machine Tools and Manufacture, 2015. **88**(0): p. 131-164.
26. Pastewka, L., et al., MRS Bulletin-Three decades of many-body potentials in materials research, 2012. **37**(5): p. 493-503.
27. Tersoff, J., *Empirical interatomic potential for silicon with improved elastic properties.* Physical Review B, 1988. **38**(14): p. 9902.
28. Daw, M.S. and M.I. Baskes, *Embedded-atom method: Derivation and application to impurities, surfaces, and other defects in metals.* Physical Review B, 1984. **29**(12): p. 6443-6453.
29. Stillinger, F.H. and T.A. Weber, *Computer simulation of local order in condensed phases of silicon.* Physical Review B, 1985. **31**(8): p. 5262-5271.
30. Stillinger, F.H. and T.A. Weber, *Erratum: Computer simulation of local order in condensed phases of silicon [Phys. Rev. B 31, 5262 (1985)]*. Physical Review B, 1986. **33**(2): p. 1451-1451.
31. Berendsen, H.J.C., J.R. Grigera, and T.P. Straatsma, *The missing term in effective pair potentials.* The Journal of Physical Chemistry, 1987. **91**(24): p. 6269-6271.
32. Tersoff, J., *New empirical approach for the structure and energy of covalent systems.* Physical Review B, 1988. **37**(12): p. 6991.

33. Tersoff, J., *Modeling solid-state chemistry: Interatomic potentials for multicomponent systems.* Physical Review B, 1989. **39**(8): p. 5566.
34. Tersoff, J., *Erratum: Modeling solid-state chemistry: Interatomic potentials for multicomponent systems.* Physical Review B, 1990. **41**(5): p. 3248.
35. Tersoff, J., *Carbon defects and defect reactions in silicon.* Physical Review Letters, 1990. **64**(15): p. 1757.
36. Tersoff, J., *Chemical order in amorphous silicon carbide.* Physical Review B, 1994. **49**(23): p. 16349.
37. Agrawal, P.M., L.M. Raff, and R. Komanduri, *Monte Carlo simulations of void-nucleated melting of silicon via modification in the Tersoff potential parameters.* Physical Review B, 2005. **72**(12): p. 125206.
38. Devanathan, R., T. Diaz de la Rubia, and W.J. Weber, *Displacement threshold energies in β-SiC.* Journal of Nuclear Materials, 1998. **253**(1–3): p. 47-52.
39. Kumagai, T., et al., *Development of bond-order potentials that can reproduce the elastic constants and melting point of silicon for classical molecular dynamics simulation.* Computational Materials Science, 2007. **39**(2): p. 457-464.
40. Bazant, M.Z., E. Kaxiras, and J. Justo, *Environment-dependent interatomic potential for bulk silicon.* Physical Review B, 1997. **56**(14): p. 8542.
41. Lucas, G., M. Bertolus, and L. Pizzagalli, Journal of Physics: Condensed Matter, 2010. **22**(3): p. 035802.
42. Baskes, M.I., J.S. Nelson, and A.F. Wright, Physical Review B, 1989. **40**(9): p. 6085-6100.
43. Brenner, D.W., Physical Review B, 1990. **42**(15): p. 9458-9471.
44. Stuart, S.J., A.B. Tutein, and J.A. Harrison, The Journal of Chemical Physics, 2000. **112**(14): p. 6472-6486.
45. van Duin, A.C.T., et al., *ReaxFF: A Reactive Force Field for Hydrocarbons.* The Journal of Physical Chemistry A, 2001. **105**(41): p. 9396-9409.
46. Erhart, P. and K. Albe, *Analytical potential for atomistic simulations of silicon, carbon, and silicon carbide.* Physical Review B, 2005. **71**(3): p. 035211.
47. Yu, J., S.B. Sinnott, and S.R. Phillpot, Physical Review B, 2007. **75**(8): p. 085311.
48. Zhou, X.W. and F.P. Doty, Physical Review B, 2008. **78**(22): p. 224307.
49. Bartók, A.P., et al., Physical Review Letters, 2010. **104**(13): p. 136403.
50. de Brito Mota, F., J.F. Justo, and A. Fazzio, *Structural properties of amorphous silicon nitride.* Physical Review B, 1998. **58**(13): p. 8323.
51. Matsunaga, K. and Y. Iwamoto, *Molecular Dynamics Study of Atomic Structure and Diffusion Behavior in Amorphous Silicon Nitride Containing Boron.* Journal of the American Ceramic Society, 2001. **84**(10): p. 2213-2219.
52. Matsunaga, K., C. Fisher, and H. Matsubara, *Tersoff Potential Parameters for Simulating Cubic Boron Carbonitrides.* Japenese Journal of Applied physics, 2000. **39**: p. L48-L51.
53. Pastewka, L., et al., *Screened empirical bond-order potentials for Si-C.* Physical Review B, 2013. **87**(20): p. 205410.
54. Pastewka, L., et al., Physical Review B, 2008. **78**(16): p. 161402.
55. Cai, M.B., et al., International Journal of Machine Tools and Manufacture, 2007. **47**(3-4): p. 562-569.
56. Brinksmeier, E. and W. Preuss, *Micro-machining.* Philosophical Transactions of the Royal Society A: Mathematical, Physical and Engineering Sciences, 2012. **370**(1973): p. 3973-3992.
57. Wang, C., et al., Proceedings of the Institution of Mechanical Engineers, Part B: Journal of Engineering Manufacture, 2014: p. 0954405414543316.
58. Cai, M.B., X.P. Li, and M. Rahman, International Journal of Machine Tools and Manufacture, 2007. **47**(1): p. 75-80.
59. Zykova-Timan, T., D. Ceresoli, and E. Tosatti, Nature Materials, 2007. **6**(3): p. 230-234.
60. Luo, X., S. Goel, and R.L. Reuben, Journal of the European Ceramic Society, 2012. **32**(12):

p. 3423-3434.
61. Komanduri, R., N. Chandrasekaran, and L.M. Raff, *Molecular dynamics simulation of atomic-scale friction.* Physical Review B, 2000. **61**(20): p. 14007-14019.
62. Komanduri, R., *Some aspects of machining with negative rake tools simulating grinding.* International Journal of Machine Tool Design and Research, 1971. **11**(3): p. 223-233.
63. Astakhov, V.P., *Fundamentals of the Selection of Cutting Tool Geometry Parameters Geometry of Single-point Turning Tools and Drills*. 2010, Springer London. p. 127-204.
64. Nakasuji, T., et al., CIRP Annals - Manufacturing Technology, 1990. **39**(1): p. 89-92.
65. Komanduri, R. and L. Raff, Proceedings of the Institution of Mechanical Engineers, Part B: Journal of Engineering Manufacture, 2001. **215**(12): p. 1639-1672.
66. Komanduri, R. and W.R. Reed Jr, Wear, 1983. **92**(1): p. 113-123.
67. Biddut A.Q., et al., *Performance of single crystal diamond tools with different rake angles during micro-grooving on electroless nickel plated die materials.* International Journal of Advanced Manufacturing Technology, 2007. **33**(0): p. 891-899.
68. Krulewich D., et al., *An empirical survey on the influence of machining parameters on tool wear in diamond turning of large single crystal silicon optics - Paper prepared for submission to ASPE 14th Annual meeting at Monterey, CA.* 1999, Lawrence Livermore National Laboratory: Livermore, USA.
69. Samuels Leonard E., Scientific American, 1978. **239**(5): p. 132.
70. Komanduri, R., et al., Philosophical Magazine Part B, 2001. **81**(12): p. 1989 - 2019.
71. Blackley, W.S. and R.O. Scattergood, *Ductile-regime machining model for diamond turning of brittle materials.* Precision Engineering, 1991. **13**(2): p. 95-103.
72. Wang, M., W. Wang, and Z. Lu, The International Journal of Advanced Manufacturing Technology, 2012. **60**(5): p. 473-485.
73. Shibata Y., F.S., Makino E. and Ikeda M., *Ductile-regime turning mechanism of single-crystal silicon.* Precision Engineering, 1996. **18**: p. 129-137.
74. Patten, J.A. and W. Gao, Precision Engineering, 2001. **25**(2): p. 165-167.
75. Patten, J., W. Gao, and K. Yasuto, Journal of Manufacturing Science and Engineering, 2005. **127**(3): p. 522-532.
76. Durazo-Cardenas, I., et al., Wear, 2007. **262**(3-4): p. 340-349.
77. Leung, T.P., W.B. Lee, and X.M. Lu, Journal of Materials Processing Technology, 1998. **73**(1-3): p. 42-48.
78. Fang, F.Z. and V.C. Venkatesh, CIRP Annals - Manufacturing Technology, 1998. **47**(1): p. 45-49.
79. Yan, J., et al., CIRP Annals - Manufacturing Technology, 2012. **61**(1): p. 131-134.
80. Inasaki, I., CIRP Annals - Manufacturing Technology, 1987. **36**(2): p. 463-471.
81. Goel, S., *PhD thesis, An atomistic investigation on the nanometric cutting mechanism of hard, brittle materials*, in *Mechanical Engineering*. 2013, Heriot-Watt University: Edinburgh. p. 1-246.
82. Ravindra, D., *Ductile mode material removal of ceramics and semiconductors*, in *Department of Mechanical and Aeronautical Engineering*. 2011, Western Michigan University: Michigan. p. 312.
83. Goel, S., X. Luo, and R.L. Reuben, Computational Materials Science, 2012. **51**(1): p. 402-408.
84. To, S., W.B. Lee, and C.Y. Chan, Journal of Materials Processing Technology, 1997. **63**(1–3): p. 157-162.
85. Pastewka, L., PhD thesis on *Multi-scale simulations of carbon nanomaterials for supercapacitors, actuators and low-friction coatings*, 2010, Fruanhofer IWM, Albert-Ludwigs-Universität, Germany: Freiburg, Germany.
86. Jonathan A. Salem, Zhuang Li, and Richard C. Bradt, *Thermal expansion and elastic anisotropy in single crystal Al2O3 and SiC Reinforcements, NASA Technical Memorandum 106516 prepared for ASME Symposium on advances in composite materials and structure*

sponsored by American society of Mechanical Engineers. December 10-12, 1986: Anaheim, California.
87. Shaw, M.C., *Metal Cutting Principles*. Oxford Series on Advanced Manufacturing, ed. J.R. Crookall, M.C. Shaw, and N.P. Suh. 2004, New York: Oxford University Press.
88. Zareena, A.R. and S.C. Veldhuis, Journal of Materials Processing Technology, 2012. **212**(3): p. 560-570.
89. Yan, J., Syoji, Katsuo, Tamaki, Jun'ichi, Wear, 2003. **255**(7-12): p. 1380-1387.
90. M. A. Davies, et al. *Application of precision diamond machining to the manufacture of micro-photonics components*. in *Lithographic and Micromachining Techniques for Optical Component Fabrication II*. 2003. San Diego, USA: SPIE.
91. Tomohiro Fukaya, et al., *High Precision Cutting of Hardened Steel with Newly Developed PCBN Tools.* accessed from imtp.free.fr/imtp2/C4/Fukaya_Tomohiro.pdf on 10/7/2011, 2011.
92. U. Grimm, et al. *Fabrication of surfaces in optical quality on pretentious tools steels by ultra precision machining.* in *Proceedings of the 4th Euspen International Conference*. 2004. Glasgow.
93. Yan, J., Z. Zhang, and T. Kuriyagawa, International Journal of Machine Tools and Manufacture, 2009. **49**(5): p. 366-374.
94. Patten J.A., *Ductile Regime Nanocutting of Silicon Nitride*, in *Proceedings ASPE 2000 Annual Meeting,*. 2000. p. 106-109.
95. Hung, N.P. and C.H. Zhong, Journal of Materials Processing Technology, 1996. **58**(1): p. 109-113.
96. John A. Patten, et al., *Chapter 2: Numerical simulations and cutting experiments on single point diamond machining of semiconductors and ceramics*, in *Semiconductor Machining at the Micro-Nano Scale*, J. Yan and J.A. Patten, Editors. 2007, Transworld Research Network: Trivandrum-695 023, Kerala, India.
97. Ravindra, D. and J.A. Patten, *Chapter 4: Ductile regime material removal of silicon carbide(SiC)*, in *Silicon Carbide: New Materials, Production methods and application*, S.H. Vanger, Editor. 2011, Nova Publishers: Trivandrum, India. p. 141-167.
98. Shayan, A.R., et al., *Force Analysis, Mechanical Energy and Laser Heating Evaluation of Scratch Tests on Silicon Carbide (4H-SiC) in Micro-Laser Assisted Machining ([micro sign]-LAM) Process.* ASME Conference Proceedings, 2009. **2009**(43611): p. 827-832.
99. Niihara, K., Journal of the Less Common Metals, 1979. **65**(1): p. 155-166.
100. Goel, S., et al., Nanoscale Research Letters, 2011. **6**(1): p. 589.
101. Belak, J., *Nanotribology: Modelling Atoms When Surfaces Collide*, in *Energy and Technology Review*. 1994, Lawrence Livermore Laboratory.
102. Komanduri, R., N. Chandrasekaran, and L.M. Raff, Wear, 2000. **242**(1–2): p. 60-88.
103. Zhiguo Wang, Y.L., Mingjun Chen, Zhen Tong, Jiaxuan Chen. *Analysis about diamond tool wear in nano-metric cutting of single crystal silicon using molecular dynamics method*. 2010: SPIE.
104. Liang, Y.C., et al. in *Nanoelectronics Conference, 2008. INEC 2008. 2nd IEEE International*. 2008.
105. Noreyan, A., J.G. Amar, and I. Marinescu, Materials Science and Engineering B-Solid State Materials for Advanced Technology, 2005. **117**(3): p. 235-240.
106. Noreyan, A. and J.G. Amar, Wear, 2008. **265**(7-8): p. 956-962.
107. Rentsch, R. and I. Inasaki, *CIRP* Annals-Manufacturing Technology, 2006. **55**(1): p. 601-604.
108. Roundy, D. and M.L. Cohen, Physical Review B, 2001. **64**(21): p. 212103.
109. Kelchner, C.L., S.J. Plimpton, and J.C. Hamilton, Physical Review B, 1998. **58**(17): p. 11085.
110. Ghafouri-Azar, R., J. Mostaghimi, and S. Chandra, Computational Materials Science, 2006. **35**(1): p. 13-26.